

Supporting Information

Ground state geometry and vibrations of polyphenylene vinylene oligomers

Nikita V. Tukachev,^{1,2} Dmitry R. Maslennikov,^{2,3} Andrey Yu. Sosorev,^{2,3} Sergei Tretiak,^{1,4}
Andriy Zhugayevych¹

¹ Center for Energy Science and Technology, Skolkovo Institute of Science and Technology, Moscow 143026, Russia

² Institute of Spectroscopy, Russian Academy of Sciences, Fizicheskaya 5, Troitsk, Moscow 108840, Russia

³ Physics Department, Moscow State University, Moscow 119991, Russia

⁴ Theoretical Division, Los Alamos National Laboratory, Los Alamos, New Mexico 87545, United States

Contents

S1. Geometric definitions	3
S2. Literature review	4
S3. Computational methodology	6
S4. Benchmarks	10
S6. Geometry and rotational constants	25
S7. PES sections and vibrational wave functions	27
S8. PES in cluster	32
S9. Vibrational spectra	33
S10. Raman spectra: experimental details and computational analysis	39
S11. Longer oligomers	41
S12. Electronic couplings and band structure	44
References	48

List of figures

S1. Orientation and atom indexing of stilbene molecule	S3
S2. PES approximation error vs basis size	S8
S3. Change of harmonic frequencies of the LAMs along two linear paths on PES	S8
S4. Correlation plots for different DFT functionals for various descriptors	S12
S5. Predicted and observed energies of vibrational transitions	S13
S6a. Benchmarking PES for torsion: basis set convergence for CAM-B3LYP	S19
S6b. Benchmarking PES for torsion: basis set convergence for MP2	S19
S6c. Benchmarking PES for torsion: CAM-B3LYP and wB97XD vs MP2 and CC	S20
S7a. Vibrational transition energies for torsion of styrene	S21
S7b. PES of the flexible dihedral of styrene	S22
S7c. ZPE and change of harmonic frequencies for styrene	S22
S7d. Benchmarking torsional PES of styrene: basis set convergence for MP2	S23
S7e. Benchmarking torsional PES of styrene: DFT vs MP2 and CC	S23
S7f. Basis set dependence of PES energies for MP2 and CCSD for styrene	S24
S8. Dependence of the rotational constants A,B,C on flexible dihedrals $\phi_{1,2}$	S25
S9. 1D paths on 2D PES of <i>trans</i> -stilbene	S27
S10a,b. 2D PES sections and wave functions by DFT/ TZVP	S28
S10c,d. 2D PES sections and wave functions by CAM-B3LYP in different basis sets	S30

S10e. 2D wave functions by CAM-B3LYP + ZPE and wB97XD in def2-TZVP basis set	S31
S11. 2D PES of trans-stilbene molecule in rigid crystal	S32
S12. 1D PES section along <i>buckling</i> β coordinate for trans-stilbene cluster 13.....	S32
S12x. Convergence of harmonic vibrational frequencies with respect to the cluster size.....	S37
S13. IR spectra of <i>trans</i> -stilbene crystal in high frequency region	S38
S13x. Linear electron-phonon couplings for all bright excited states of the planar stilbene	S40
S14. Band structure for electrons (a) and holes (b) in stilbene.....	S45
S15. Band structure for electrons (a) and holes (b) in OPV5	S47

List of tables

S1. Notations for stilbene conformers.	S3
S2. Notations for nonplanar PPV conformers.	S3
S3. Vibrational (τ and β) transition energies	S13
S4. Basis sets sizes	S14
S5a,b. Descriptors for <i>trans</i> -stilbene: NBO charges, QCT, BLA, τ and β	S15
S6a,b. Descriptors for <i>trans</i> -stilbene: frequencies of Raman-active modes.....	S17
S7. Descriptors for <i>trans</i> -stilbene: lowest Hessian eigenvalues	S18
S8. Torsional vibrational levels for styrene in a gas phase.....	S21
S9. Comparison of geometry structure of trans-stilbene in different environments.....	S24
S10. Observed BLA in crystals	S25
S11. Important dihedrals and rotational constants of <i>trans</i> -stilbene	S26
S12. Frequencies of Raman-active vibrational modes in vacuum and in crystal	S33
S13. Frequencies of Raman-active vibrational modes in crystal: below 400 cm ⁻¹	S33
S14. Physical interpretation of the lowest vibrational modes.....	S34
S15. Vibrational frequencies (in meV) of various systems: molecule to crystal.....	S35
S16. Interpretation of low-frequency Raman active modes	S36
S16x. Lowest excitations of the planar trans-stilbene calculated by TDDFT	S40
S17. Conformer energies in meV	S41
S18. Lowest vibrational frequencies in meV in fully planar geometry	S42
S19. Calculated vs. experimental geometry of OPV crystals.....	S43
S20. Hopping amplitudes: stilbene vs TCNQ	S44
S21. Transfer integrals and efficiencies for electrons and holes in stilbene crystal	S44
S22. Transfer integrals and efficiencies for electrons and holes in OPV5 crystal.....	S46

S1. Geometric definitions

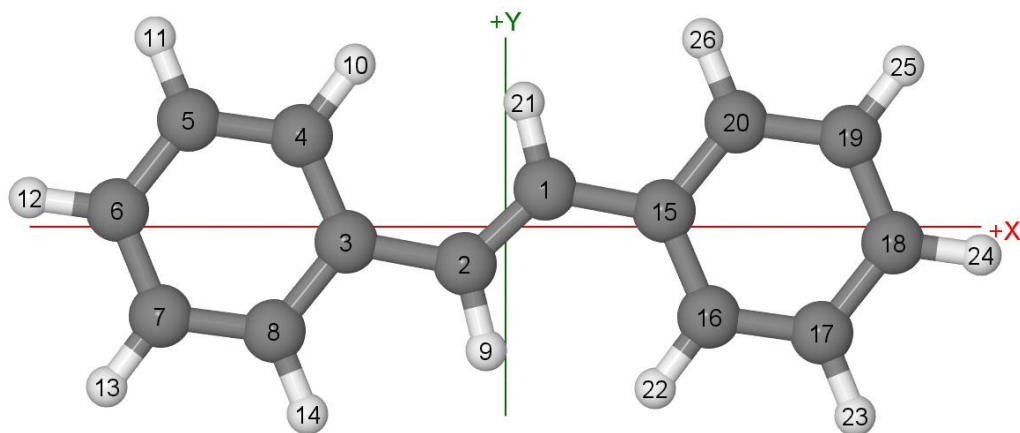


Figure S1. Orientation and atom indexing of stilbene molecule used in this work.

Table S1. Notations for stilbene conformers. Here $\phi_{1,2}$ are the angles between the rings and the vinyl group or approximately the dihedrals (1,2,3,4) and (2,1,15,16), $\tau=(\phi_1+\phi_2)/2$ is the torsion angle which is the half-angle between the rings, and $\beta=(\phi_1-\phi_2)/2$ is the buckling angle which is the angle between the vinyl group and the mean plane of the two rings. The three stationary (by symmetry) points are labeled below as 'p', 's', 't'. The 's'-point is the middle point for rotation of individual dihedrals: depending on method it can be either saddle or shallow local minimum.

label	ϕ_1	ϕ_2	τ	β	symmetry	comment
p	0	0	0	0	2/m	planar
a	τ_0	τ_0	τ_0	0	2	torsion minimum
b	β_0	$-\beta_0$	0	β_0	-1	buckling minimum
s	90	0	45	45	m	high-symmetry saddle
t	90	-90	0	90	2/m	PES maximum

Table S2. Notations for nonplanar PPV conformers. String of signs denotes signs of flexible dihedrals in the order from one side of the oligomer to the other side.

label	dihedrals pattern	symmetry	comment
OPV2 (stilbene)			
a	++	2	torsion
b	+-	-1	buckling
OPV3 (distyrylbenzene)			
a	++++	2	helical torsion
b	+--+	-1	alternating buckling
c	+-+-	2	helical buckling
d	++--	-1	alternating torsion
OPV5			
ax	++++----	-1	1 defect (ax1)
bx	+--+--+-+	2	
cx	+--+--+-	-1	
dx	++-----++	2	2 defects (ax2)

S2. Literature review

Geometry of trans-stilbene in gas phase. Experimentally, the geometry of *trans*-stilbene was determined by means of gas electron diffraction [10]. By studying the squared error sum and standard deviation values for the refined parameters as functions of the C–C(Ph) torsion angles, the authors of Ref. [10] concluded that $\beta=0$, $\tau\approx 30^\circ$, and $\text{BLA}=0.13\text{--}0.15\text{ \AA}$. In another work [11], free jet microwave spectra were used to obtain rotational constants for *trans*-stilbene assuming C_{2h} (2/m) symmetry: $A=2611.3\pm 7.7\text{ MHz}$, $B=262.86\pm 0.02\text{ MHz}$, and $C=240.56\pm 0.02\text{ MHz}$. First principle calculations at different levels of theory predict the same value for constants B and C, but different values of other parameters: constant A larger by approximately 100 MHz, BLA closer to the lower experimental value, and range of dihedrals from zero to a value smaller than 30° . In particular, Ref.[17] reports CCD/6-31G* estimate of BLA to be 0.131 \AA , and for butadiene the same method underestimates experimental value only by 0.002 \AA [S1]. Thus, available experimental gas phase techniques did not provide a robust direct determination of BLA and flexible dihedrals. At the other hand, published ab initio methods HF and MP2 overestimate BLA ($\sim 0.150\text{ \AA}$), whereas commonly used B3LYP underestimates it ($\sim 0.120\text{ \AA}$).

Geometry of PPV crystals. In a solid state, experimental data are available for crystals of *trans*-stilbene (OPV2) [23], distyrylbenzene (OPV3) [19], OPV5 [20], and PPV [21–22]. Unfortunately, thus determined values of BLA (see Table S10) are mutually inconsistent and do not follow a known systematic trend: BLA decreases with increase of the distance from terminal ends of the π -conjugated system [S2]. Concerning the dihedrals, all oligomers and the polymer are reported to be flat within the experimental uncertainty, though large thermal fluctuations of dihedrals were observed in Ref.[22]. This is consistent with very small deplanarization energy gain (if any), so that intermolecular steric interactions easily planarize the molecules. Noticeably, crystal structures of short oligomers (OPV2 and OPV3) show unavoidable disorder in molecular orientation [21,26,30]. It is unclear whether this disorder is dynamic or frozen, because the two orientations are connected via pedaling rotation of the vinyl group, which is not constrained sterically.

Vibrations of stilbene molecule: high frequencies. Vibrational spectra of the *trans*-stilbene were investigated both experimentally [S3,13,27] and theoretically [S3,13–14,16,S4,28]. In Ref.[27] the gas phase Raman spectrum was recorded at 330°C using a specially constructed high temperature cell allowing to observe and assign low-frequency vibrational modes. In work [S3] infrared and Raman spectra of microcrystalline *trans*-stilbene were measured and the vibrational frequencies were assigned using gas-phase force constants calculations with scaling adopted from benzene and ethylene. Later, infrared and Raman spectra of *trans*-stilbene in solution (n-hexane, benzene) and in powder were reported [13], complemented by DFT B3LYP/6-311+G** calculations of vibrational frequencies as well as corresponding Raman activities, Raman depolarization ratios, and infrared intensities. The variety of quantum chemistry methods, including MP2 and DFT (B3LYP) in Pople basis sets of different quality, was used in work [14] to obtain the vibrational frequencies of *cis*- and *trans* isomers. Infrared and Raman spectra simulations of *cis*- and *trans*-stilbene were also carried out in works [16] and [S4]. Comparative estimation of vibrational frequencies, obtained in the harmonic approximation with scaling, was reported at B3LYP/cc-pVTZ level of theory in Ref [28]. For high frequency region ($>400\text{ cm}^{-1}$), Raman spectra of *trans*-stilbene are reported to be quite well reproduced by harmonic approximation with scaled B3LYP frequencies [13,27]. For longer OPVs, frequencies of some vibrations estimated by means of Franck–Condon analysis of the fluorescence emission spectra as well as estimated BLA values are discussed in Ref. [30]. In work [S5] combined experimental and theoretical investigation of Raman-resonant and nonresonant third-order susceptibilities of OPVn ($n=1\text{--}5$) was carried out. Raman spectra of PPV are dominated by two strong Raman bands [S5,25,31]: the band at 1600 cm^{-1} corresponds to the BLA mode [S6] and the band at 1200 cm^{-1} has more complex nature. The relative Raman intensities were reported to be affected by the chain length of the molecules only slightly [25]. The BLA mode band typically shows triplet structure [S5,25,31], with the intensity ratio $R(\text{band } 1/\text{band } 3)$ increasing with the chain length [31].

Vibrations of stilbene molecule: low frequencies. In contrast to high-frequency vibrations, LAMs require determination of PES beyond the harmonic approximation. In literature there are a few works investigating the shape of PES of PPV oligomers. Authors of Ref.[14] noted that, according to MP2 computations made, the nonplanar conformation of *trans*-stilbene is usually preferred, contradicting B3LYP results. One-dimensional minimum energy path along the phenyl ring rotation coordinate for the *trans*-stilbene molecule was calculated at the B3LYP/cc-pVDZ level of theory in Ref.[16] and refined by MP2 and B3LYP in cc-pVTZ in Ref.[17]. Transition frequencies observed in the fluorescence excitation and dispersed fluorescence spectra were used to determine the parameters of the two-dimensional PES ($\phi_{1,2}$) for the ground and excited states of *trans*-stilbene [32]. The potential parameters obtained for the ground state were improved in work [S7]. Finally, B3LYP/6-31G* calculations [33] were performed to obtain the theoretical two-dimensional potential surface, which was further refined by using the observed energy level spacing taken from the literature. In Ref. [34] the role of ZPE correction on the PES shape is investigated at MP2/6-31G** level of theory and it is stressed that the molecule is effectively planar with respect to rotation of the vinyl fragment about the longitudinal axis (pedaling motion). Overall, the topology of the two-dimensional PES for *trans*-stilbene molecule *in vacuo* is known, but quantitative details are missing including position and energy of minima and saddle points. Consequently the comparison of torsion progression observed experimentally and calculated from first principles reveals significant discrepancies. Also, no investigations of PES in non gas phase conditions (e.g. in solid state) has been published.

Vibrations of stilbene crystal. Experimental IR and Raman spectra of *trans*-stilbene crystal have been reported and analyzed in Refs.[S8,35,36]. Detailed and consistent analysis of high-frequency region was made in [S8], basing on symmetry considerations and of wave-number shifts of ten deuterated species as well as previous assignments made for substituted benzenes. For low-frequency part, peak at 59 cm^{-1} was assigned to B_g torsion accordingly to previous assignment of the first overtone at 127.7 cm^{-1} in the Raman spectrum of gaseous styrene [S9]. Authors [S8] stated, however, that in some cases the assignment was tentative and normal coordinate analysis is necessary. Paper [36] was focused on the analysis of low-frequency part of the Raman spectrum based on symmetry considerations and comparison with fluorescence spectra. It was pointed out that each A_g and B_g mode of the free molecule may split in the solid into four components, two with A_g and two with B_g , symmetry, and all four factor-group components may appear in the Raman spectrum of the solid. They also stated, however, that the similarity transformation that connects the polarizability derivatives of the molecule and the solid (in the oriented gas model) is such that no unambiguous assignments of the symmetries of molecular modes can be made. A few points of interest were discussed in Ref.[36] with the first one concerning the assignment of 129 cm^{-1} line. Some investigators assigned it to the lowest A_g fundamental since this line is common to the Raman and the fluorescence spectrum, whereas the authors assigned it to the overtone of the B_g torsional fundamental. Another issue stated is that the lines in the Raman spectrum of the powder can be divided into two groups according to their linewidth. The sharp lines can be understood in terms of nearly harmonic fundamentals which give rise to a few weak combination bands. On the other hand, broad bands could be attributed to an accidental quasi-degeneracy of a number of combinations and overtones of very anharmonic low frequency fundamentals. Qualitative analysis of all notable Raman-active peaks below 600 cm^{-1} was made in Ref.[36] basing on the assumption that the stronger components represent A_g and the weaker components represent B_g overtones or combinations; the lowest possible set of vibrational quantum numbers to satisfy the observed intensity alternation was proposed and anharmonicity constants were estimated by RMS fit of observed data. Thus, the authors assumed that the low-frequency Raman spectrum could be rationalized as an A_g and B_g overtones or combinations of torsional coordinates that are anharmonic in the solid and strongly coupled. However, first principle simulations for *trans*-stilbene vibrational spectra in crystal have not been reported yet.

S3. Computational methodology

Calculations of equilibrium geometry parameters and harmonic vibrational frequencies of PPV oligomers are performed by DFT with various exchange-correlation energy functionals commonly applied to π -conjugated molecules: PBE, HSE06, B3LYP, CAM-B3LYP, LC- ω PBE, ω B97XD, APFD, M06-2X. Used for the majority of calculations in present work, CAM-B3LYP is a long-range corrected hybrid functional known to provide a correct description of molecular and electronic structure of extended π -conjugated systems [S10,S11,40,41]. Dispersion interactions (for crystalline environment simulations) are taken into account by means of Grimme’s dispersion model with Becke-Johnson damping [42]. Majority of computations for free molecule and molecular clusters is made in 6-31G* and def2-TZVP basis sets. Solid-state DFT computations with the plane-wave basis set are performed with PAW pseudopotentials and 600 eV energy cutoff. Γ -centered $4\times 7\times 3$ Monkhorst-Pack k -grid is utilized for geometry optimizations of trans-stilbene and phonon frequencies calculations. Geometry parameters are optimized with tight convergence criteria predefined in both Gaussian and VASP programs. Phonon frequencies are estimated in harmonic approximation at Γ -point. Raman scattering factors were evaluated by means of corrected vasp_raman.py script [S12] which uses the VASP package as backend; lines broadening was simulated by gaussians.

ZPE correction. To calculate ZPE correction to PES, it is important to identify modes which can intermix with the two studied LAMs. For trans-stilbene molecule there are four low-frequency modes separated from the rest of the modes by frequency gap: the maximum frequency of the lowest four modes at any PES point does not exceed 17 meV, whereas the frequency of the 5th mode is 25 meV. The four lowest modes are torsion (A_u), buckling (B_g), out-of-plane bending (A_u), and in-plane bending (B_u), where the symmetry is given for the planar geometry. These modes are identified at any point of the PES by matching normal mode displacements (through eigenvector overlap) of the two vinyl carbon atoms at that point and at the fully planar geometry (alternative method of mode tracking along a linear path fails at points where buckling and in-plane bending modes intermix). Visual analysis of modes has been used to confirm the reliability of this approach near level crossing points. The dependence of ZPE and frequency of the four lowest modes on τ and β is shown in Fig. S3, and the resulting ZPE-corrected PES is given in Fig. 2b.

Calculations for crystals. Periodic boundary conditions substantially restrict the variety of available computational methods. Among the already discussed methods, PBE-D3 is the only one having efficient implementation in periodic boundary conditions. For CAM-B3LYP-D3 we will use a hybrid scheme explored in our previous work [41]: for optimization of intermolecular packing we use PBE-D3 and then perform cluster calculations with frozen perimeter using CAM-B3LYP-D3. Molecular crystals of short PPV oligomers with resolved structure possess unavoidable conformational disorder [19,23]. In the present work we use the dominant conformer from Ref. [23] to obtain a fully relaxed (unit cell and atomic positions) by DFT-D geometry and then explore conformational space in cluster calculations. Unit cell parameters optimized by PBE-D3, PBE-MBD, vdW-DF2 are listed in Table S19. All the three methods give geometry close to the experimental one within few percent accuracy. In what follows we will use PBE-D3 geometry for two reasons: it best matches experimental geometry and out of the three it is the only method available for use with gaussian basis sets (to see the influence of basis set).

Solution of 2D vibrational problem. For the two LAMs the anharmonic vibrational problem is solved following the approach introduced in Refs. [S13,S14,39]. For a set of LAMs defined by the coordinates $(\varphi_1, \dots, \varphi_n)$ we use the model Hamiltonian

$$H(\varphi_1, \dots, \varphi_n) = -\frac{1}{2} \sum_{i=1}^n \sum_{j=1}^n \frac{\partial}{\partial \varphi_i} B_{ij}(\varphi_1, \dots, \varphi_n) \frac{\partial}{\partial \varphi_j} + V(\varphi_1, \dots, \varphi_n) \quad (\text{S1})$$

where n is the dimension of the problem, $B_{ij} = B_{ji}$ are kinematic parameters, and V is the potential function. The kinematic matrix is given by

$$B = (Y - X^T I^{-1} X)^{-1} \quad (\text{S2})$$

where I stands for inertia tensor and blocks X and Y effectively account for rotation-vibration interactions and interactions between different vibrations, respectively:

$$X_{qi} = \sum_k m_k \left(\vec{r}_k \times \frac{\partial \vec{r}_k}{\partial \phi_i} \right)_q \quad Y_{ij} = \sum_k m_k \left(\frac{\partial \vec{r}_k}{\partial \phi_i} \right) \cdot \left(\frac{\partial \vec{r}_k}{\partial \phi_j} \right) \quad (\text{S3})$$

where m_k , r_k are mass and position of k -th atom, and $q=x,y,z$ enumerates cartesian coordinates. Partial derivatives are evaluated by numerical differentiation. For stilbene $n=2$ with the angles $\varphi_{1,2}$ defined in Table S1. The potential V is periodic in each φ_i with the period 180° and

$$V(\varphi_1, \varphi_2) = V(-\varphi_1, -\varphi_2) \quad (\text{S4})$$

Both B_{ij} and V are calculated on a grid with step size 5° and then approximated by trigonometric functions of the variables φ_i considering symmetry requirements:

$$B_{ij}(\varphi_1, \varphi_2) = \sum_K \sum_L C_{ijKL}^{\alpha_1 \alpha_2} f_K^{\alpha_1}(\varphi_1) f_L^{\alpha_2}(\varphi_2) \quad (\text{S5})$$

$$V(\varphi_1, \varphi_2) = \sum_K \sum_L V_{KL}^{\alpha_1 \alpha_2} f_K^{\alpha_1}(\varphi_1) f_L^{\alpha_2}(\varphi_2) \quad (\text{S6})$$

where $f_K^\alpha(\varphi)$ denotes $\cos K\varphi$ or $\sin K\varphi$ depending on the parity α . In a constrained geometry optimization by Gaussian program the angles $\varphi_{1,2}$ are approximated by the dihedrals (1,2,3,4) and (2,1,15,16), but the symmetry is preserved by sampling only the fundamental domain $0 \leq \varphi_1 \leq \pi/2$, $\varphi_2 < |\varphi_1|$. We use 12-order harmonics to fit V (the resulting RMS error is about 1 cm^{-1}), 6-order to fit B and ZPE, and 20-order for wave-function. The Hamiltonian (S1) is solved by variational method. Note that the lowest vibrations are fully confined within ± 40 -degree rectangle around the $\varphi_{1,2}=0$ point. The assignment of vibrational levels (i.e. determination of vibrational quantum numbers) is performed by the analysis of localization areas of wave-function and structure of its nodal surfaces.

Marginal probability distributions are calculated from vibrational wave-function $\chi(\alpha_1, \alpha_2)$ as follows:

$$f(\alpha_1) = \frac{\int_{-\pi/k}^{\pi/k} |\chi(\alpha_1, \alpha_2)|^2 d\alpha_2}{\int_0^{\pi/k} \int_{-\pi/k}^{\pi/k} |\chi(\alpha_1, \alpha_2)|^2 d\alpha_1 d\alpha_2} \quad (\text{S7})$$

where α_1, α_2 correspond to either symmetrized coordinates (τ, β) (in that case, $k=4$) or dihedrals $\varphi_{1,2}$ ($k=2$).

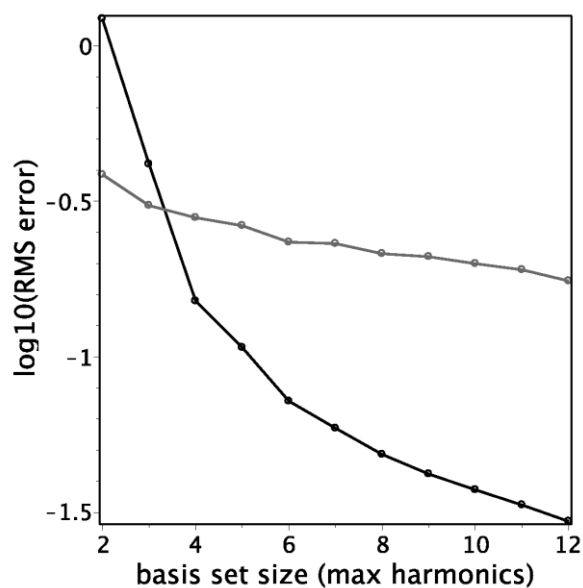


Figure S2. Dependence of the PES approximation error on the size of the trigonometric basis: total energy (black line) and ZPE correction (gray line) calculated by CAM-B3LYP/6-31G* method.

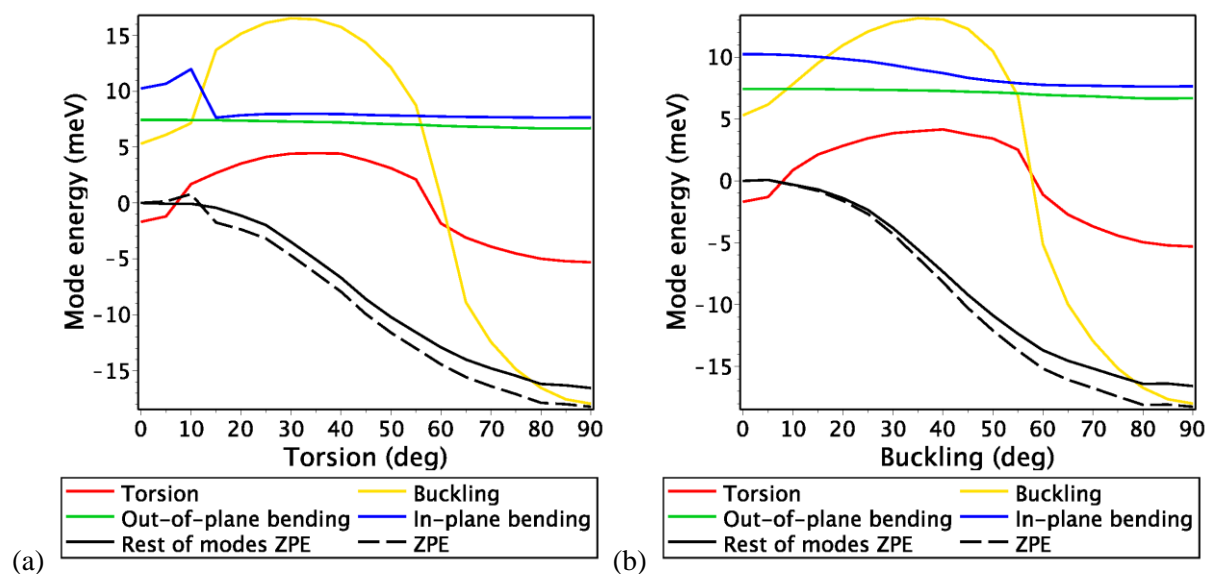


Figure S3. ZPE and change of harmonic frequencies of the LAMs along two linear paths on the two-dimensional PES: (a) along torsion and (b) along buckling. The ZPE correction used in this work is shown by dashed line.

Perturbation theory for vibrations of molecular clusters and solids.

Consider a quadratic Hamiltonian

$$H = \frac{1}{2} \sum_{\alpha} M_{\alpha} \dot{x}_{\alpha}^2 + \frac{1}{2} \sum_{\alpha\beta} U''_{\alpha\beta} x_{\alpha} x_{\beta}, \quad (\text{S8})$$

where x_{α} are dynamic variables (coordinates), \mathbf{M} is the mass matrix, and \mathbf{U}'' is the force constants matrix. If $\{\mathbf{\Lambda}, \mathbf{T}\}$ are the eigenelements of the spectral problem

$$\mathbf{U}'' \mathbf{T} = \mathbf{M} \mathbf{T} \mathbf{\Lambda} \quad (\text{S9})$$

(the orthonormalization is $\mathbf{T}^{\top} \mathbf{M} \mathbf{T} = \mathbf{1}$) then the transformation

$$x_{\alpha} = \sum_{\beta} T_{\alpha\beta} \sqrt{\frac{\hbar}{\omega_{\beta}}} \xi_{\beta}, \quad \xi_{\beta} = \sqrt{\frac{\omega_{\beta}}{\hbar}} \sum_{\alpha} x_{\alpha} M_{\alpha} T_{\alpha\beta} \quad (\text{S10})$$

diagonalizes the vibrational Hamiltonian:

$$H = \frac{1}{2} \sum_{\alpha} \hbar \omega_{\alpha} (\pi_{\alpha}^2 + \xi_{\alpha}^2 \text{sgn } \Lambda_{\alpha}), \quad (\text{S11})$$

here $\omega_{\alpha} = \sqrt{|\Lambda_{\alpha}|}$, $\pi_{\alpha} = \dot{\xi}_{\alpha}/\omega_{\alpha}$, and both ξ and π are dimensionless.

Now let $\mathbf{U}'' = \mathbf{U}''_0 + \mathbf{V}$ and $\mathbf{U}''_0 \mathbf{T}_0 = \mathbf{M} \mathbf{T}_0 \mathbf{\Lambda}_0$. Then the vibrational modes of \mathbf{U}'' are given by the following eigenvalue problem

$$\check{\mathbf{U}} \check{\mathbf{T}} = \check{\mathbf{T}} \mathbf{\Lambda}, \quad \text{where } \check{\mathbf{U}} = \mathbf{T}_0^{\top} \mathbf{U}'' \mathbf{T}_0 \equiv \mathbf{\Lambda}_0 + \mathbf{T}_0^{\top} \mathbf{V} \mathbf{T}_0, \quad \mathbf{T} = \mathbf{T}_0 \check{\mathbf{T}}, \quad \text{and } \check{\mathbf{T}}^{\top} \check{\mathbf{T}} = \mathbf{1}. \quad (\text{S12})$$

In the present work, \mathbf{U}'' is taken from Gaussian (for molecular clusters) or VASP calculations (for molecular crystals). Two types of perturbations are considered. In the first type the unperturbed system is a free molecule in vacuum and the perturbed system is the same molecule in a rigid cluster. Then the matrix $\check{\mathbf{T}}$ shows how that rigid molecular environment distorts vibrational modes of the free molecule. In the second type the perturbed system is the crystal unit cell with the periodic boundary conditions (Γ -point calculations), whereas for the unperturbed system we set all intermolecular elements of the force constant matrix to zero. Then the matrix $\check{\mathbf{T}}$ gives vibrational modes of the crystal in the basis of vibrations of individual molecules, see for example Table S16.

S4. Benchmarks

Because PPV oligomers are among the most studied π -conjugated molecules with complex PES highly sensitive to computation method, they are excellent objects for benchmarking of DFT methods. In this work we use several descriptors sensitive to the computational method.

BLA and bond orders. An important and sensitive descriptor to monitor the polarization and charge transfer in conjugated molecules is BLA (Table S5a). Since PBE is universal GGA method and as such is known to provide only a limited accuracy, for system in question it delivers only a zero-approximation results that more specialized functionals are expected to improve: i.e., it provides the lowest estimation for BLA and highest charge transfer integral from vinyl C=C to C-C(Ph) bond. The problem could be attributed to well-known self-interaction issue that is common for semi-local functionals. B3LYP, as an empirical hybrid functional extensively parameterized for organic molecules, quite expectedly improves on all quantities tested compared to PBE and yet it still provides rather poor estimation for BLA value. Since CAM-B3LYP functional was specifically designed to resolve known B3LYP deficiencies on charge transfer it allows to obtain BLA quite close to experiment while also maintaining effectively planar equilibrium structure for trans-stilbene and reproducing experimentally observed torsion progression [32] close to spectroscopic accuracy (≈ 1 cm⁻¹). Other tested hybrid functionals with the long-range correction, ω B97XD and LC- ω PBE, also provide an accurate BLA but yield nonplanar structure for trans-stilbene (Fig. 3c) and fail to reproduce observed torsion frequencies (Fig. 3e, Table S3). For Raman-active vibrations (Table S6a) one can note that known systematic tendency of PBE to underestimate harmonic vibrational frequencies holds; moreover, the method provides the lower limit among all functionals tested. It seems unclear why the upper limit is given by CAM-B3LYP estimations, whether that is a systematic trend or coincidence. We believe it requires detailed investigation and leave the matter without explanation.

Lowest vibrational states of *trans*-stilbene in vacuum. We benchmark methods upon experimentally observed energies of the lowest vibrational transitions [32] (up to fourth overtone for torsion vibration). In particular, from Fig. 3e and Fig. S5 it can be seen that the best estimations for torsion frequencies are obtained for APFD and CAM-B3LYP functionals (8 and 6 cm⁻¹ vs 8 in experiment for the fundamental transition). As one could expect, density functionals predicting single-minimum PES (PBE, B3LYP) systematically overestimate transition energies, whereas functionals showing both buckling and deep torsion minima (ω B97XD, LC- ω PBE, M06-2X, MP2) underestimate them.

The dependence of the CAM-B3LYP results on basis set is noncritical: Fig. 5b shows that 6-31G*, 6-311G*, TZVP, def2-TZVP (closest to basis set convergence limit) give consistent results. Also the results are insensitive with respect to addition of the D3 dispersion correction. Effectively taking into account other vibrations by adding ZPE correction (in harmonic approximation) to the PES also does not change the results qualitatively (observable distribution of angles) but renormalizes the PES and thus the vibrational energy levels, see Figs. 2-3 and Table S3. For these reasons and because the computational overhead of using large basis sets and making ZPE correction is substantial, in the rest of the study we will use CAM-B3LYP/6-31G* without ZPE (whose predicted transition energies are close to CAM-B3LYP/def2-TZVP with ZPE), but with D3 correction whenever is important.

It should be noted that (1,0) transition can be missed in analysis of experimental spectra if its frequency is close to zero as predicted by such methods as ω B97XD. In this case the entire ω B97XD curve in Fig. 5a will be displaced to the left so that calculated (n,0) transition matches observed (n-1,0) transition. However, the slope of the curve remains the same and, evidently, it does not follow the experimental slope. A completely different approach to provide reference data for DFT methods would be to use CC calculations. Unfortunately, for post Hartree-Fock methods the PES converges slowly with increasing basis set, see Fig. S6b, whereas commonly used methods "accelerating" this convergence (see e.g. [S15]) are not suitable for providing meV-accuracy for

Å-scale deviations in geometry. For MP2 in particular, consistent results are observed only for the largest considered basis sets: aug-cc-pVTZ, cc-pVQZ and def2-QZVP. Fortunately, the basis set dependence is systematic: upon basis set increase the entire PES shifts up relative to (0,0) point. Therefore the calculated CCSD/def2-TZVP energies for MP2/def2-TZVP geometry are expected to provide the lower bound for PES. Thus generated one-dimensional cross-section of the PES along the torsion coordinate coincides with ω B97XD/6-31G*, see Fig. S6c. MP2 results in large basis sets are close to ω B97XD/def2-TZVP. For both cases, the dihedral distribution for the ground state wave-function is shown in Fig. 3. In particular, ω B97XD/def2-TZVP predicts effectively planar geometry but with broad distribution of angles compared to CAM-B3LYP results because the underlying PES has shallow minima at $\tau \approx 15^\circ$. Though ω B97XD/def2-TZVP predicts broader distribution of angles compared to CAM-B3LYP both correspond to effectively planar geometry of trans-stilbene.

Empirical PES. Based on our extensive DFT benchmarking of the PES, we have also tested the empirical model proposed in Ref. [32] which assumes relatively simple 4th-order harmonic trigonometric form of the potential function. It turns out that upon addition of higher harmonics to PES expansion, the expansion coefficients and approximation error decrease in magnitude gradually, with 4th order being the minimum meaningful order, see Fig. S2.

Conclusions. HSE06 hybrid specifically designed to describe solids for trans stilbene performs close to B3LYP, slightly improving PES but predicting less accurate BLA. M06-2X results are always close to ω B97XD as should be expected since both were parameterized for similar use (thermochemistry, noncovalent interactions) and test sets. APFD functional designed for accurate (comparable to CC) description of weak dispersive interactions and hydrogen bonds allows to reproduce PES section along torsions well (Fig. 5a), but shows surprisingly small value for BLA and hence is less desirable studying conjugated systems than CAM-B3LYP. MP2 fails to deliver consistent results for trans-stilbene especially for small (double- and triple-zeta) basis sets: BLA is too small (Table S5a), the equilibrium geometry is severely distorted, PES seems too complex for 2D section by just two dihedrals [S16] to be meaningful.

Our data show that common systematic trends for DFT calculations work for trans-stilbene. CAM-B3LYP provides best DFT estimations for a chosen set of descriptors compared to available experimental and CC data. APFD could probably be used for conformational analysis of organic molecules but should be avoided when accurate description of charge transfer matters. On the contrary, ω B97XD works well for those systems but does not allow to reproduce PES consistently at 6-31G* basis set. It should be mentioned that for the free molecule dispersion interactions seem fairly negligible (Tables S5a,S6a). It should be emphasized that neither CAM-B3LYP nor other DFT methods especially in small basis sets are usually suitable for calculations within 1 cm^{-1} accuracy. If the study demands the use of DFT, it should be benchmarked against relevant experimental data to choose the viable option for further investigation.

The analysis of the dependence of descriptors (most importantly, BLA and frequencies of torsion and buckling modes, Tables S5b,S6b) on the basis set coupled with CAM-B3LYP calculations identifies three groups of basis sets: accurate but large, small but inaccurate, small and accurate. The largest basis sets of each family (def2-QZVP, 6-311+G(3df,2p), cc-pVQZ) show good level of consistency thus indicating a basis set convergence. Benchmarked by these three basis sets, we see that only 6-31G* basis set gives a reasonable balance of size and accuracy. If accuracy is important, def2-TZVP stands as the smallest fault-free basis set which provides results close to complete basis set, but it is two times larger than 6-31G*.

Comparing lowest frequencies estimated for different PPV oligomers one could see that DFT trends discussed above for stilbene hold also for oligomers (Table S18): CAM-B3LYP and APF data are caught between PBE-like methods and B3LYP (upper bound) and ω B97XD (lower bound). As for the geometry in crystal, both PBE-D3 and vdW-DF2 yield satisfactory results (the former predict slightly lesser unit cell volume while the latter overestimates it as shown in Table S19).

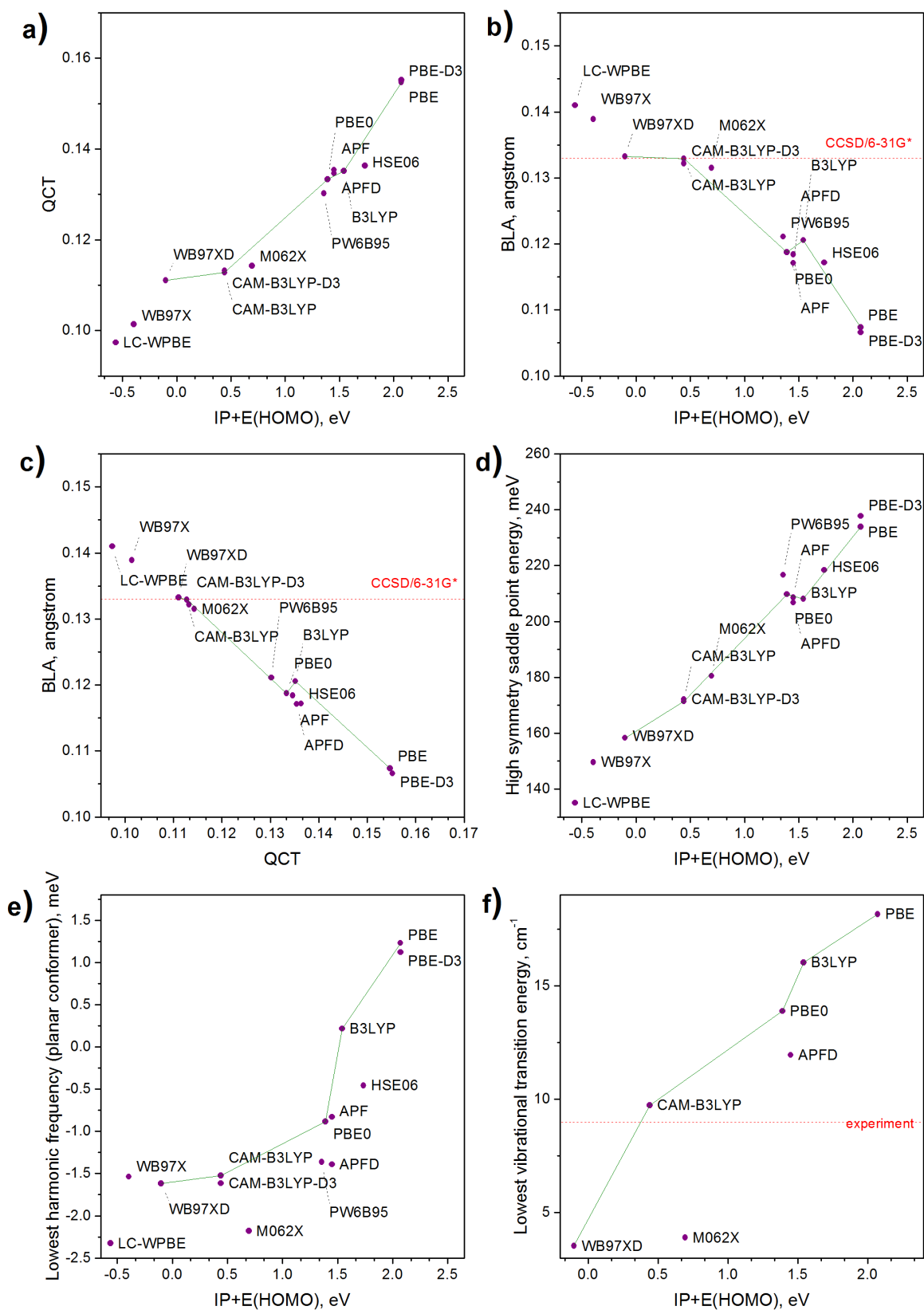


Figure S4. Correlation between IP+EHOMO descriptor and key properties of the stilbene molecule calculated with different density functionals at def2-TZVP basis set. The QCT is the charge transfer associated with the BLA: it is calculated as the bond order deficiency for the vinyl double bond, i.e. 2 minus NBO bond order.

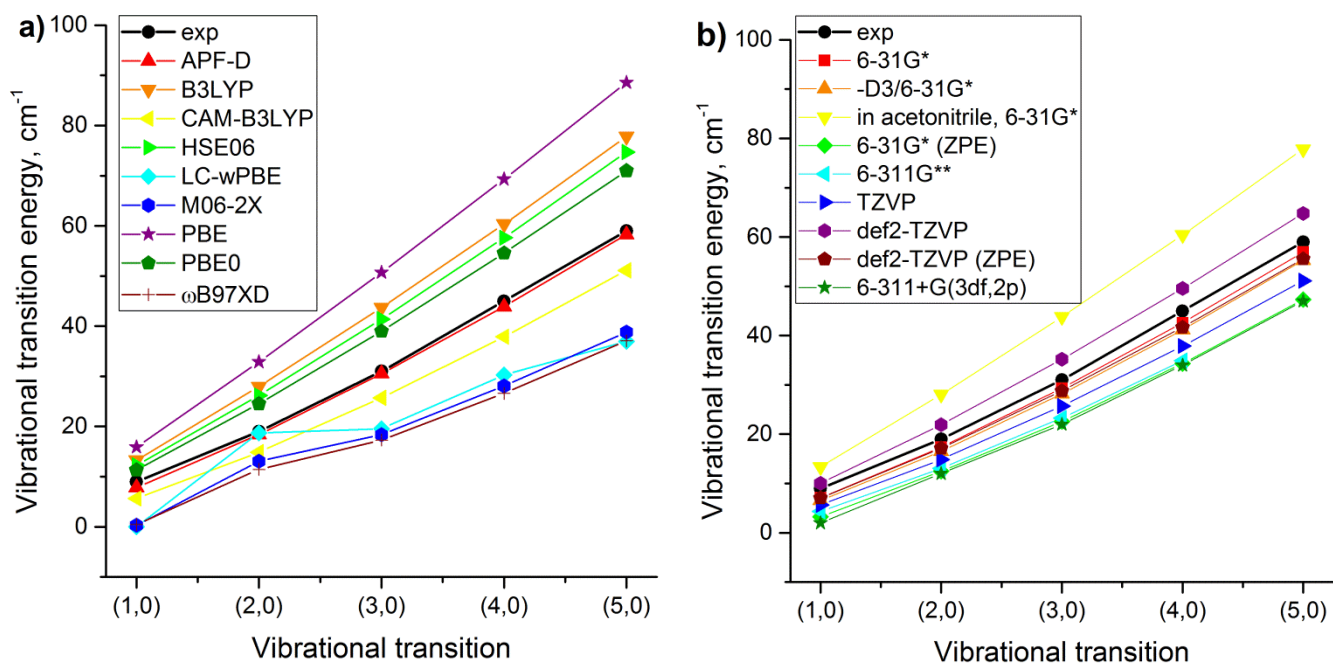


Figure S5. Predicted and observed energies of vibrational transitions for a) different DFT functionals with TZVP basis set and b) CAM-B3LYP functional but different basis sets, accounting for dispersion interactions and highly polar dielectric environment.

Table S3. Vibrational transitions energies (in cm^{-1} , beyond harmonic approximation) from zero vibrational level for torsion and buckling vibrations as appeared in experiment and DFT. In the notation (v_1, v_2) , the first quantum number corresponds to torsion τ , and the second one to buckling β vibration.

	(1,0)	(2,0)	(3,0)	(4,0)	(5,0)	(0,1)
exp	9	19	31	45	59	53
TZVP						
ω B97XD	0	11	17	27	37	54
LC- ω PBE	0	19	20	30	37	57
M06-2X	0	13	18	28	39	59
CAM-B3LYP	6	15	26	38	51	61
APF-D	8	18	31	44	58	74
HSE06	12	26	41	58	75	77
B3LYP	13	28	44	60	78	78
PBE	16	33	51	69	89	84
CAM-B3LYP						
6-311+G(3df,2p)	2	12	22	34	47	58
6-311G**	4	13	23	35	48	58
6-31G*(ZPE)	3	12	23	34	47	61
-D3/6-31G*	7	17	28	41	55	63
def2-TZVP (ZPE)	7	17	29	42	56	64
6-31G*	7	17	29	43	57	64
def2-TZVP	10	22	35	50	65	66
acn 6-31G*	13	28	44	60	78	71

Table S4. Sizes of basis sets used in this work (as reported in Gaussian 16 program). Basis sets used in the present work are highlighted.

Basis set	basis	cartesian	primitive
6-31G	150	150	356
6-31G*	234	234	440
cc-pVDZ	256	270	546
def2-DZVP	256	270	434
6-311G*	288	302	508
6-311G**	324	338	544
6-311+G*	344	358	564
6-311+G(2d,p)	450	478	684
def2-TZVP	506	576	810
cc-pVTZ	588	670	932
6-311+G(3df,2p)	654	738	944
aug-cc-pVTZ	920	1070	1332
cc-pVQZ	1130	1400	1690
def2-QZVP	1158	1428	1744

Table S5a. Descriptors for *trans*-stilbene: NBO charges on H22 and H9, charge transfer from double to single bonds calculated as bond order deficiency of the double bond, BLA, torsion τ and buckling β angles for conformers *a* and *b* (if non-planar) and their relative energies taken with opposite sign, relative energies of saddle point $E_{(90,0)}$ and PES maximum $E_{(90,90)}$. Rows are ordered by IP+EHOMO. For vdW-DF2/PAW600 the BLA is 0.113 Å. Methods used in the present work are highlighted.

Method	IP+EHOMO eV	QH22	QH9	QCT	BLA Å	τ deg	E_a meV	β deg	E_b meV	$E_{(90,0)}$ meV	$E_{(90,90)}$ meV
6-31G*											
PBE-D3	2.13	0.239	0.229	0.154	0.103					253	465
PBE	2.13	0.240	0.229	0.153	0.104					249	459
HSE06	1.79	0.239	0.229	0.134	0.114	6.7	0.1			224	413
B3LYP	1.60	0.230	0.220	0.133	0.117					222	412
APF	1.50	0.239	0.229	0.133	0.116	8.4	0.3			213	396
APFD	1.50	0.239	0.229	0.133	0.114	11.1	1.1			212	391
PBE0	1.44	0.240	0.230	0.131	0.116	8.9	0.4			214	398
PW6B95	1.41	0.233	0.222	0.129	0.118	8.8	0.4			222	414
M062X	0.75	0.236	0.225	0.112	0.128	17.0	5.5			187	354
CAM-B3LYP-D3	0.49	0.232	0.222	0.111	0.129	13.1	1.7			185	347
CAM-B3LYP	0.49	0.232	0.222	0.111	0.130	12.5	1.4			184	347
ω B97XD	-0.05	0.237	0.226	0.109	0.130	19.3	6.8	9.4	0.4	164	311
ω B97X	-0.34	0.234	0.223	0.100	0.136	18.6	5.9	9.6	0.5	158	301
LC- ω PBE	-0.51	0.240	0.230	0.095	0.138	21.8	10.2	15.4	1.8	138	264
CCSD		0.226	0.214	0.168	0.130	26.9	24.2*	25.1	15.9	107	207
MP2		0.231	0.219	0.175	0.112	26.6	29.2	24.9	19.7	131	251
def2-TZVP											
PBE-D3	2.07	0.210	0.200	0.155	0.107					238	432
PBE	2.07	0.210	0.200	0.155	0.107					234	426
HSE06	1.74	0.208	0.197	0.136	0.117					218	400
B3LYP	1.54	0.201	0.190	0.135	0.121					208	381
APF	1.45	0.208	0.197	0.135	0.118					209	383
APFD	1.45	0.208	0.197	0.135	0.117	5.3	0.3			207	379
PBE0	1.39	0.209	0.198	0.133	0.119					210	386
PW6B95	1.36	0.203	0.192	0.130	0.121					217	400
M062X	0.69	0.206	0.195	0.114	0.132	14.1	2.9			180	338
CAM-B3LYP-D3	0.44	0.203	0.192	0.113	0.132	9.8	0.6			172	320
CAM-B3LYP	0.44	0.203	0.192	0.113	0.133	9.0	0.5			171	320
ω B97XD	-0.10	0.204	0.193	0.111	0.133	15.6	2.7			158	298
ω B97X	-0.40	0.203	0.192	0.101	0.139	14.8	2.1			150	284
LC- ω PBE	-0.56	0.211	0.198	0.097	0.141	19.2	5.6	10.5	0.5	135	257
MP2		0.202	0.191	0.191	0.111	17.1	6.6	11.0	2.2	175	330

* For this geometry: CCSD(T)/6-31G* value is 20.2, CCSD/def2-TZVP value is 1.9.

Table S5b. Descriptors for *trans*-stilbene: basis set dependence. The largest basis set of each family is shown in boldface. Methods are ordered by the last column. Rest of the notations are described in Table S5a.

Method	IP+EHOMO eV	QH22	QH9	QCT	BLA Å	τ deg	E_a meV	β deg	E_b meV	$E_{(90,0)}$ meV	$E_{(90,90)}$ meV
CAM-B3LYP											
6-31G		0.240	0.229	0.111	0.127	8.9	0.4			194	366
def2-DZVP		0.221	0.210	0.113	0.129	0	0			196	366
6-31G*		0.232	0.222	0.111	0.130	12.5	1.4			184	347
cc-pVDZ		0.225	0.214	0.113	0.129	0	0			181	341
aug-cc-pVTZ		0.201	0.189	0.113	0.133	6.1	0.3			175	327
cc-pVTZ		0.199	0.188	0.114	0.133	10.0	0.6			174	325
cc-pVQZ		0.208	0.197	0.112	0.134	10.3	0.7			173	322
def2-QZVP		0.211	0.200	0.112	0.134	9.8	0.6			173	322
def2-TZVP		0.203	0.192	0.113	0.133	9.0	0.5			171	320
6-311+G(3df,2p)		0.204	0.192	0.111	0.133	11.0	1.5			167	310
6-311G**		0.200	0.190	0.112	0.133	15.2	2.7			161	302
6-311+G(2d,p)		0.203	0.191	0.112	0.134	12.5	2.1			160	301
6-311G*		0.198	0.188	0.112	0.133	16.7	3.6			156	292
6-311+G*		0.202	0.189	0.112	0.133	14.6	2.7			154	290

Table S6a. Harmonic vibrational frequencies of important vibrational modes of *trans*-stilbene: ν_t , ν_β stand for torsion and buckling vibrational modes, respectively, ν_5 is the mode separating the four low-frequency modes from the rest of modes, "R" denotes Raman-active modes with the subscript indicating approximate position of that mode. Rows are ordered by IP+HOMO. Imaginary frequencies are marked by 'minus' sign.

Method	IP+EHOMO eV	ν_t meV	ν_β meV	ν_5 meV	R ₁₀₀₀ cm ⁻¹	R ₁₂₀₀ cm ⁻¹	R ₁₃₀₀ cm ⁻¹	R _{1600L} cm ⁻¹	R _{1600H} cm ⁻¹
6-31G*									
PBE-D3	2.13	1.55	9.37	25.06	987	1201	1335	1611	1656
PBE	2.13	1.63	9.57	24.90	985	1198	1334	1609	1653
HSE06	1.79	-0.73	7.83	25.61	1019	1237	1379	1679	1727
B3LYP	1.60	0.84	8.50	25.58	1015	1223	1382	1655	1706
APF	1.50	-1.11	7.43	25.53	1017	1234	1378	1676	1724
APFD	1.50	-1.58	6.32	26.07	1017	1237	1385	1675	1726
PBE0	1.44	-1.14	7.30	25.62	1019	1237	1380	1683	1731
PW6B95	1.41	-1.74	7.32	26.00	1018	1238	1384	1686	1734
M062X	0.75	-2.04	3.14	26.05	1018	1238	1381	1694	1754
CAM-B3LYP-D3	0.49	-1.78	4.82	26.05	1031	1243	1394	1701	1760
CAM-B3LYP	0.49	-1.69	5.30	25.93	1029	1241	1394	1699	1758
ω B97XD	-0.05	-2.16	-2.95	25.62	1026	1237	1392	1697	1752
ω B97X	-0.34	-2.24	-3.34	26.31	1029	1243	1393	1714	1776
LC- ω PBE	-0.51	-2.75	-5.81	25.83					
CCSD		-3.44	-11.16	24.72					
MP2		-3.80	-12.73	24.11	1021	1244	1396	1672	1710
def2-TZVP									
PBE-D3	2.07	1.12	8.56	24.79	989	1191	1317	1592	1639
PBE	2.07	1.23	8.78	24.62	987	1188	1316	1590	1636
HSE06	1.74	-0.46	7.90	25.42	1020	1227	1360	1659	1709
B3LYP	1.54	0.22	8.12	25.42	1018	1208	1370	1636	1689
APF	1.45	-0.83	7.59	25.31	1019	1224	1359	1657	1706
APFD	1.45	-1.39	6.51	25.88	1020	1227	1363	1656	1708
PBE0	1.39	-0.89	7.38	25.39	1020	1227	1360	1663	1713
PW6B95	1.36	-1.36	7.08	25.69	1022	1228	1363	1666	1717
M062X	0.69	-2.18	3.72	26.27	1021	1228	1375	1674	1735
CAM-B3LYP-D3	0.44	-1.61	4.89	25.96	1034	1234	1383	1681	1742
CAM-B3LYP	0.44	-1.52	5.35	25.84	1032	1231	1383	1680	1739
ω B97XD	-0.10	-1.62	2.58	25.71	1026	1226	1379	1677	1735
ω B97X	-0.40	-1.54	2.77	26.29	1028	1232	1381	1693	1756
LC- ω PBE	-0.56	-2.33	-4.27	25.73					
MP2		-3.03	-9.85	25.26	1013	1224	1361	1638	1676

Table S6b. Continuation of Table S6a: basis set dependence. Rows are ordered by " v_{β} " column

Method	IP+EHOMO eV	v_{τ} meV	v_{β} meV	v_5 meV	R_{1000} cm^{-1}	R_{1200} cm^{-1}	R_{1300} cm^{-1}	R_{1600L} cm^{-1}	R_{1600H} cm^{-1}
CAM-B3LYP									
6-311G*		-2.12	2.53	25.86	1030	1231	1388	1686	1744
6-311G**		-2.02	3.01	25.80	1028	1229	1378	1681	1739
6-311+G(2d,p)		-1.98	4.59	25.81	1032	1228	1383	1676	1734
cc-pVQZ		-1.62	5.13	25.84	1032	1230	1383	1678	1737
cc-pVTZ		-1.54	5.15	25.82	1033	1231	1383	1680	1739
6-31G*		-1.69	5.30	25.93	1029	1241	1394	1699	1758
def2-TZVP		-1.52	5.35	25.84	1032	1231	1383	1680	1739
def2-QZVP		-1.49	5.53	25.84	1033	1230	1383	1677	1736
6-311+G(3df,2p)		-1.76	5.84	25.84	1019	1227	1381	1676	1737
6-311+G*		-1.14	6.03	25.81	1029	1230	1387	1682	1740
aug-cc-pVTZ		-1.54	6.82	25.80	1033	1230	1382	1677	1737
6-31G		-1.19	6.93	26.20	1050	1256	1420	1700	1762
cc-pVDZ		0.58	7.82	25.60	1024	1231	1356	1691	1749
def2-DZVP		1.56	9.46	25.62	1023	1233	1356	1697	1754

Table S7. Four lowest Hessian eigenvalues (in cm^{-1} , rotations are excluded) at high-symmetry points.

	(0, 0)				(90, 0)				(90, 90)			
DFT/TZVP												
APFD	13i	49	57	82	8i	124i	55	65	43i	148i	54	60
B3LYP	2i	64	58	81	13	119i	56	66	41i	144i	55	61
CAM-B3LYP	15i	38	59	82	12i	116i	57	67	40i	137i	55	62
HSE06	10i	61	58	81	10	123i	56	65	43i	147i	55	60
LC- ω PBE	23i	42i	60	82	22i	116i	57	67	39i	131i	55	61
M06-2X	13i	36i	57	87	14i	126i	57	66	39i	146i	57	61
PBE	8	69	56	78	18	122i	54	63	43i	149i	53	58
ω B97XD	13i	21i	59	82	18i	119i	56	66	40i	137i	52	61
CAM-B3LYP												
6-31G*	12i	45	60	83	8i	121i	57	67	42i	144i	54	62
-D3/6-31G*	19i	37	59	82	16i	123i	56	66	45i	146i	52	60
def2-TZVP	10i	47	60	82	3	114i	57	67	40i	139i	55	62
6-31G*(acn)	6i	49	61	82	14	120i	57	67	43i	152i	53	62

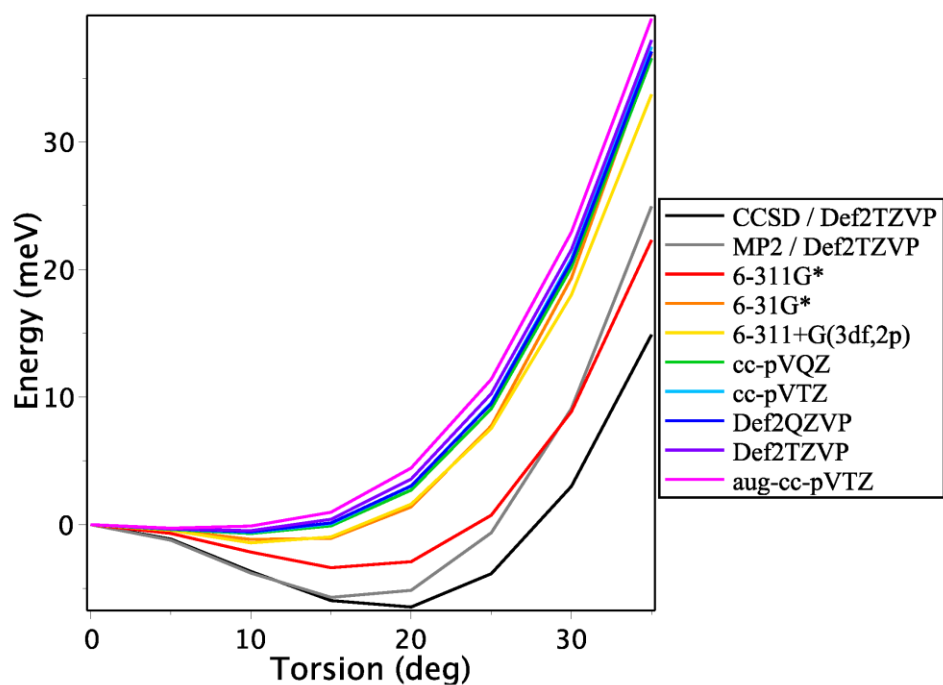


Figure S6a. Benchmarking PES for torsion: basis set convergence for CAM-B3LYP compared to CCSD and MP2 results at fixed basis set. The PES geometry is relaxed by CAM-B3LYP/def2-TZVP.

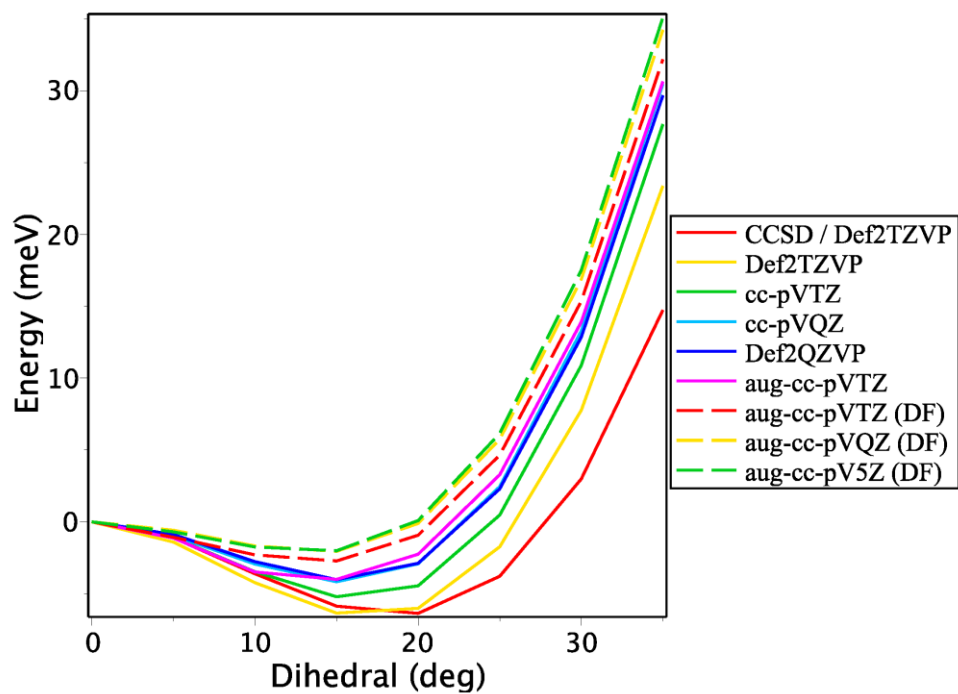


Figure S6b. Benchmarking PES for torsion: basis set convergence for MP2. The PES geometry is relaxed by MP2/def2-TZVP. The results for MP2/6-31G* are out of scale. "DF" means density fitting.

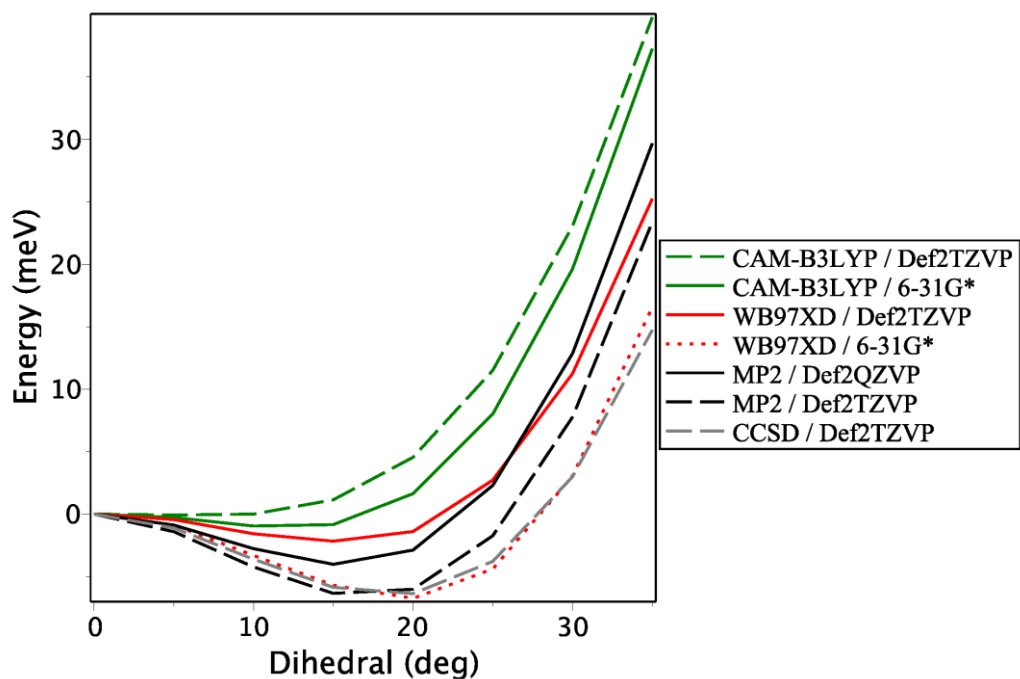


Figure S6c. Benchmarking PES for torsion: CAM-B3LYP and ω B97XD vs. MP2 and CCSD (small basis set only). The PES geometry is relaxed by MP2/def2-TZVP. Although basis set convergence has not been achieved for CCSD, comparison with MP2 allows to speculate that the converged CCSD curve will be close to ω B97XD/def2-TZVP. Also, note that in contrast to CAM-B3LYP, a large basis set is required for ω B97XD (6-31G* is insufficient).

Table S8. Calculated vs. experimental [S17] torsional vibrational levels for styrene in a gas phase. Rows are ordered by the first vibrational level. Here ν_1 is harmonic frequency of the planar conformer.

Method	Basis set	IP+EHOMO, eV	ν_1 , cm^{-1}	Vibrational levels, cm^{-1}					
PBE	6-31G*	2.65	49	61	129	203	280	359	441
PBE	def2-TZVP	2.56	45	58	123	195	268	344	422
B3LYP	6-31G*	1.99	43	56	120	191	264	340	419
B3LYP	def2-TZVP	1.91	41	55	117	186	257	330	405
HSE06	def2-TZVP	2.09	37	53	114	183	253	326	402
PW6B95	def2-TZVP	1.70	36	53	114	183	254	328	406
PBE0	def2-TZVP	1.72	34	51	111	178	247	319	394
CAM-B3LYP	def2-TZVP	0.65	21	44	98	158	222	289	358
CAM-B3LYP	6-31G*	0.72	19	44	99	161	226	295	367
APFD	def2-TZVP	1.79	20	43	98	160	225	295	367
APFD	6-31G*	1.87	-12	41	95	157	222	292	365
CAM-B3LYP+ZPE	def2-TZVP		7	39	90	148	209	273	340
CAM-B3LYP+ZPE	6-31G*		-13	39	91	150	212	278	347
experiment				38	86	139	196	255	307
M062X	def2-TZVP	0.91	12	35	85	144	205	271	340
ω B97X	def2-TZVP	-0.28	-25	35	83	137	196	258	322
ω B97XD	def2-TZVP	0.08	-31	34	83	139	198	261	328
M062X	6-31G*	0.97	-17	32	82	139	200	267	336
ω B97XD+ZPE	def2-TZVP		-33	31	77	130	187	248	311
ω B97XD	6-31G*	0.16	-42	30	77	132	191	254	321
LC- ω PBE	def2-TZVP	-0.48	-35	27	71	121	175	234	295
MP2	def2-TZVP		-47	24	71	123	179	240	304

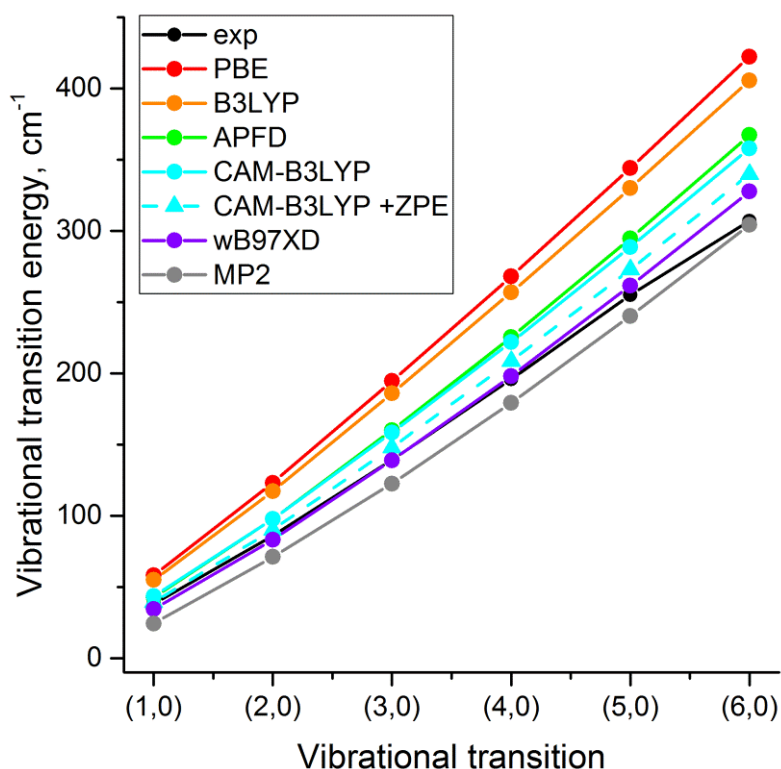


Figure S7a. Graphical representation of a subset of Table S8. The basis set is def2-TZVP.

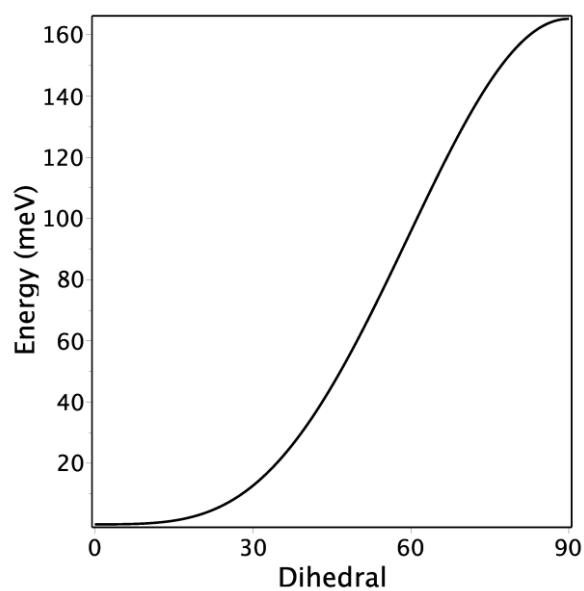


Figure S7b. PES of the flexible dihedral of styrene calculated by CAM-B3LYP/6-31G* without ZPE.

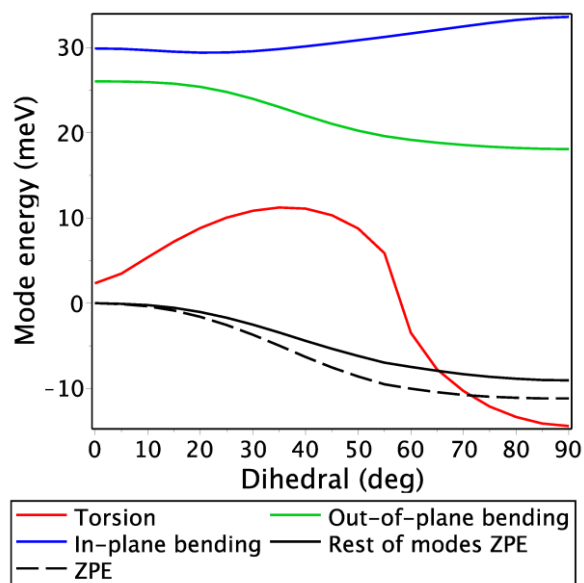


Figure S7c. ZPE and change of harmonic frequencies of the lowest vibrations along the one-dimensional PES of styrene. The ZPE correction used in this work is shown by dashed line.

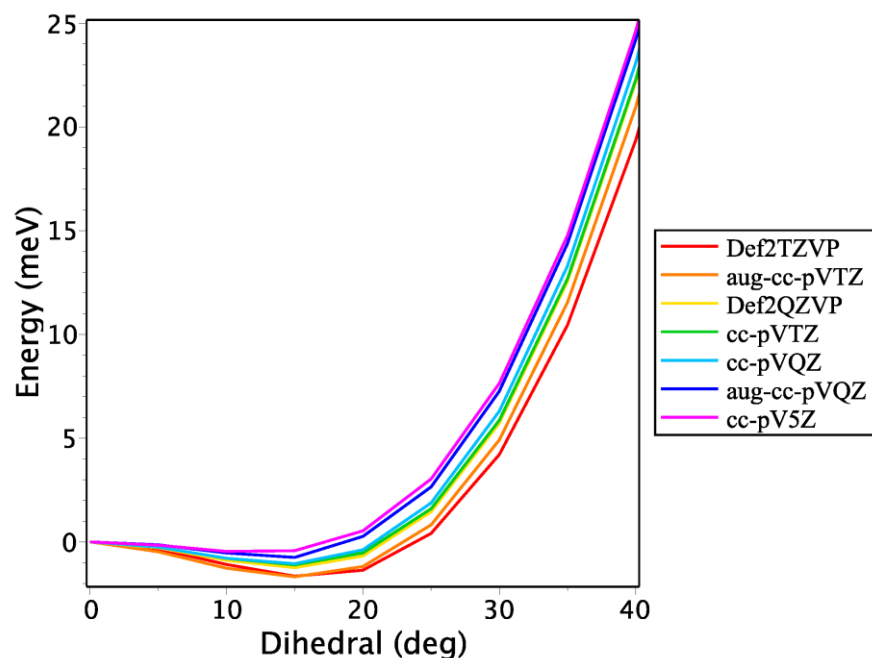


Figure S7d. Benchmarking torsional PES of styrene: basis set convergence for MP2. The PES geometry is relaxed by MP2/def2-TZVP.

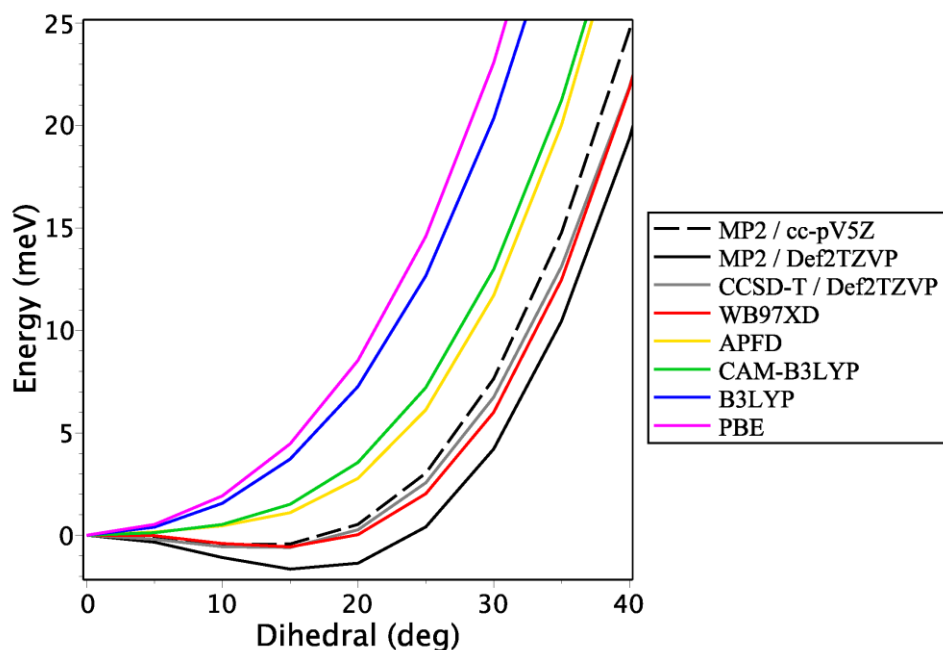


Figure S7e. Benchmarking torsional PES of styrene: various density functionals at 6-31G* basis set vs. MP2 at large basis set vs. MP2 and CCSD-T at def2-TZVP basis set. The PES geometry is relaxed by MP2/def2-TZVP. Although basis set convergence has not been achieved for CCSD-T, comparison with MP2 allows to speculate that the converged CCSD-T curve will be somewhere in between CAM-B3LYP and ω B97XD.

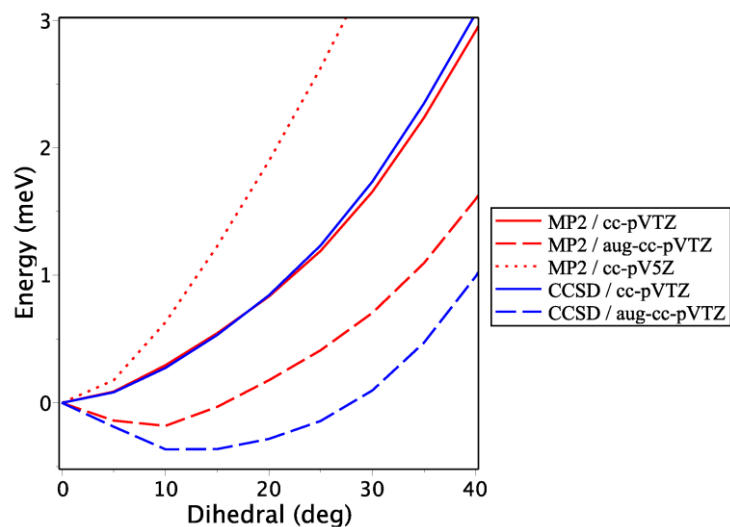


Figure S7f. Basis set dependence of PES energies (relative to the planar conformation) for MP2 and CCSD: plotted here is the difference from def2-TZVP value.

Table S9. Comparison of geometry structure of trans-stilbene in different environments.

Method	Environment	BLA, Å	Dihedrals, deg.			Inertia defect
			Θ	τ	β	
CAM-B3LYP/6-31G*	gas	0.130	180.0	12.4	0.0	-16.18
CAM-B3LYP/6-31G*	in acetonitrile	0.130	180.0	4.5	0.0	-2.13
CAM-B3LYP-D3/6-31G*	crystalline (PBE-D3)	0.127	180.0	0.0	5.0	-0.26

S6. Geometry and rotational constants

Table S10. Observed BLA in crystals. Disorder groups are distinguished by prime. Experimental estimates of BLA in gas is 0.13-0.15 Å [10].

crystal	molecule	vinyl group number			
		1	2	3	4
OPV5 relaxed by PBE-D3	1	0.099	0.092	0.092	0.099
	2	0.098	0.092	0.092	0.098
OPV5 [20]	1	0.272	0.221	0.221	0.272
	2	0.150	0.198	0.211	0.213
OPV3 [19]	1	0.242	0.245		
	1'	0.145	0.147		
	2	0.222	0.224		
	2'	0.156	0.159		
	3	0.245	0.245		
	3'	0.134	0.134		
	4	0.194	0.194		
	4'	0.171	0.171		
OPV2 [23] (est90k3 dataset)	1	0.144			
	1'	0.081			
	2	0.135			

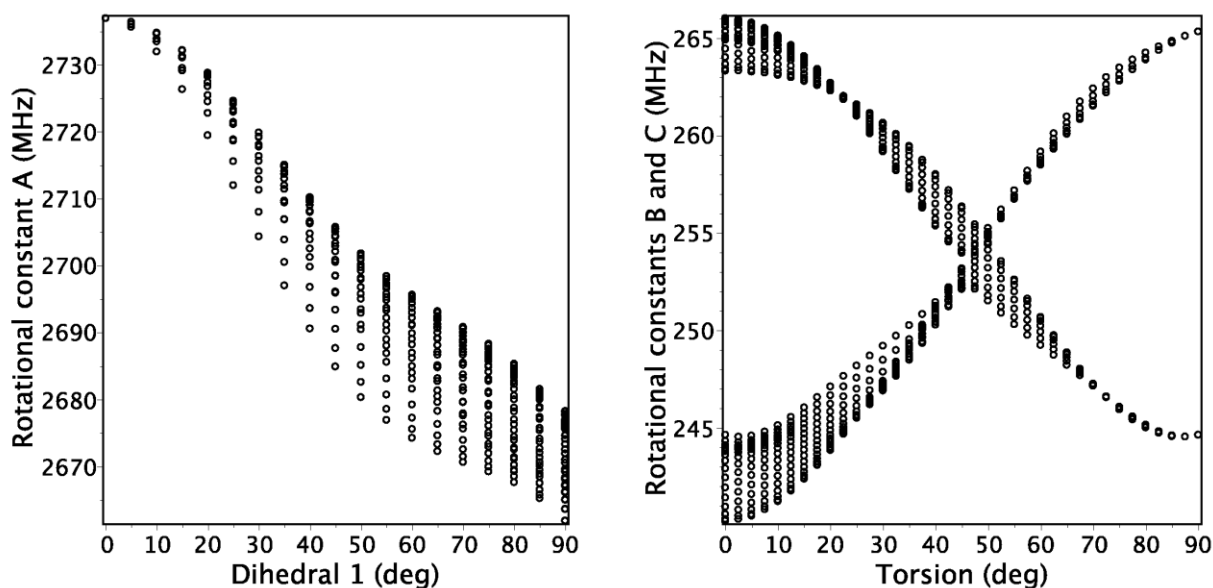


Figure S8. Dependence of the rotational constants A,B,C on flexible dihedrals $\phi_{1,2}$.

Table S11. Important dihedrals and rotational constants of *trans*-stilbene as obtained by DFT and MP2. Dihedrals Θ (C3-C2-C1-C15) and τ in microwave studies are assumed to be 180 and 0 deg., respectively, corresponding to planar structure. Experimental estimations for rotational constants A, B and C are 2611.3 ± 7.7 , 262.86 ± 0.02 , 240.56 ± 0.02 MHz [11].

DFT functional	Θ , deg.	τ , deg.	rotational constants, MHz		
			A	B	C
6-31G*					
PBE	180.0	0.0	2687	260	237
B3LYP	180.0	0.0	2715	261	238
HSE06	-179.8	5.7	2725	263	240
APF-D	-179.7	11.1	2714	263	241
CAM-B3LYP	-179.7	12.4	2730	263	242
M06-2X	-179.7	17.1	2712	263	243
LC- ω PBE	-179.9	21.8	2725	263	245
ω B97XD	-179.6	19.4	2713	262	243
B2PLYPD	-179.6	13.4	2704	262	241
MP2	-179.0	26.6	2680	261	246
TZVP					
PBE	180.0	0	2704	261	238
B3LYP	-179.8	6.5	2731	262	240
HSE06	-179.7	7.3	2741	265	242
APF-D	-179.7	6.4	2732	264	242
CAM-B3LYP	-179.9	12.9	2747	264	243
M06-2X	-179.6	18.7	2727	264	245
LC- ω PBE	179.9	22.4	2740	264	246
ω B97XD	-179.6	22.5	2726	262	245
B2PLYPD	-179.7	19.9	2709	263	244
MP2	180.0	30.0	2685	262	248
def2-TZVP					
B3LYP	-179.9	3.4	2737	263	240
APF-D	-179.9	6.4	2739	265	242
CAM-B3LYP	180.0	8.7	2756	265	243
LC- ω PBE	179.7	22.4	2748	265	246
ω B97XD	178.9	14.3	2736	264	243

S7. PES sections and vibrational wave functions

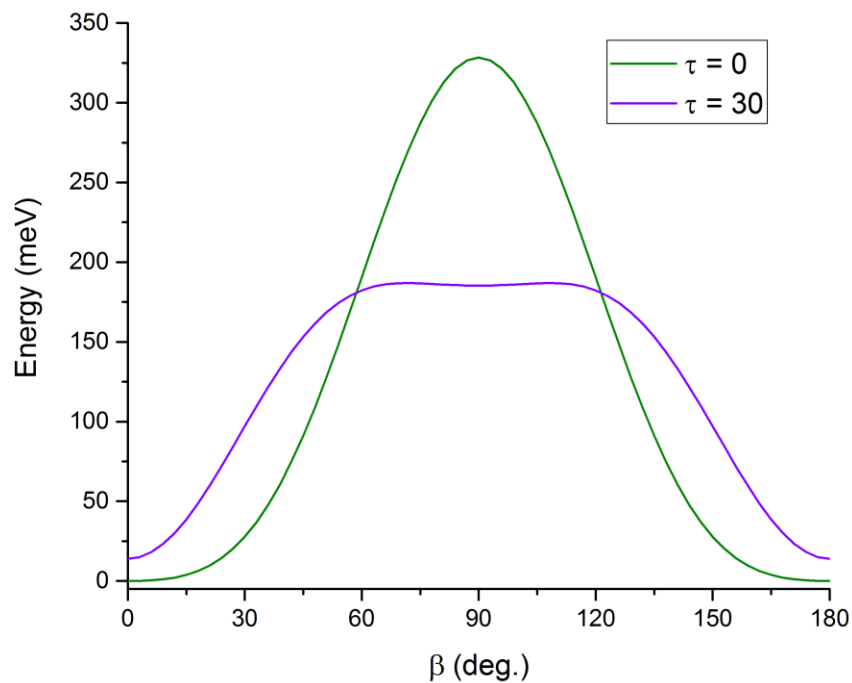


Figure S9. 1D paths for pedaling motion of vinyl group of *trans*-stilbene calculated by CAM-B3LYP-D3/6-31G* with ZPE correction. In a gas phase the pedaling flip ($\tau=0$, β is changing) proceeds via the PES maximum at 0.3 eV thus hampering the flip. Nevertheless there exists a path around that point requiring about 30-degree torsion but with the barrier below 0.2 eV.

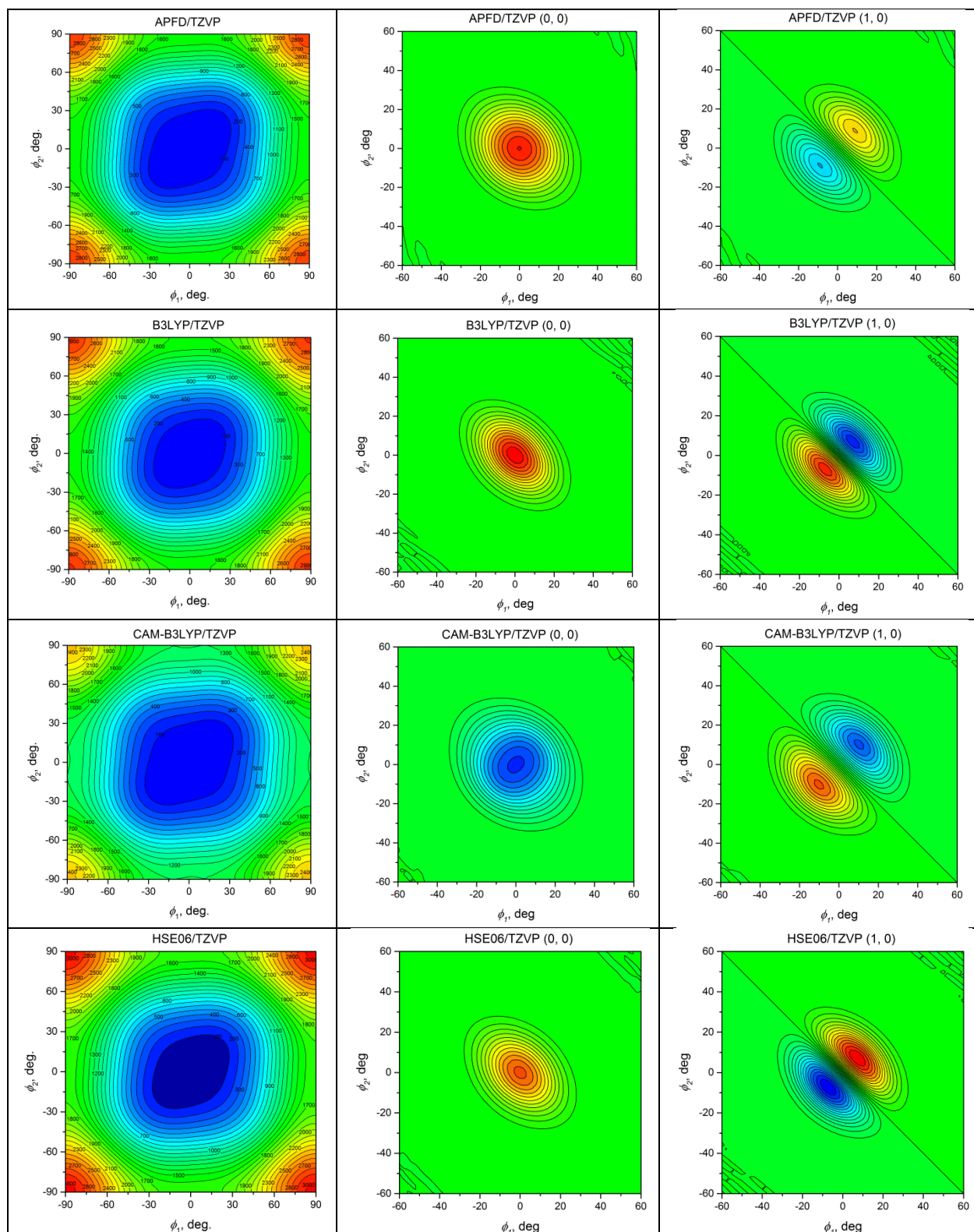


Figure S10a. 2D PES sections along ϕ_1 and ϕ_2 dihedrals and vibrational wave functions obtained for zero and first vibrational levels obtained by different DFT functionals in TZVP basis set: functionals predicting single minimum.

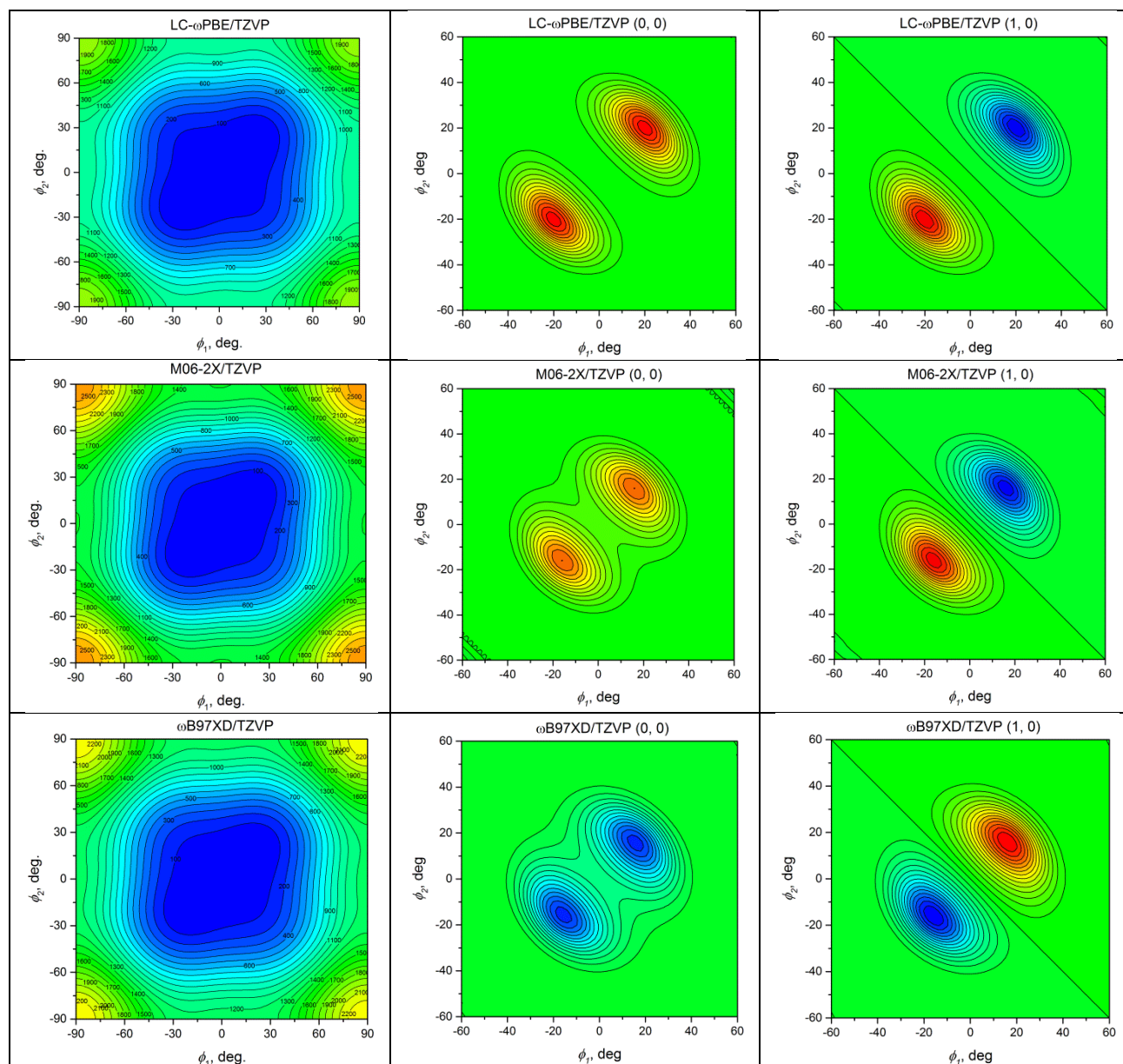


Figure S10b. 2D PES sections along ϕ_1 and ϕ_2 dihedrals and vibrational wave functions obtained for zero and first vibrational levels obtained by different DFT functionals in TZVP basis set: functionals predicting multiple minima.

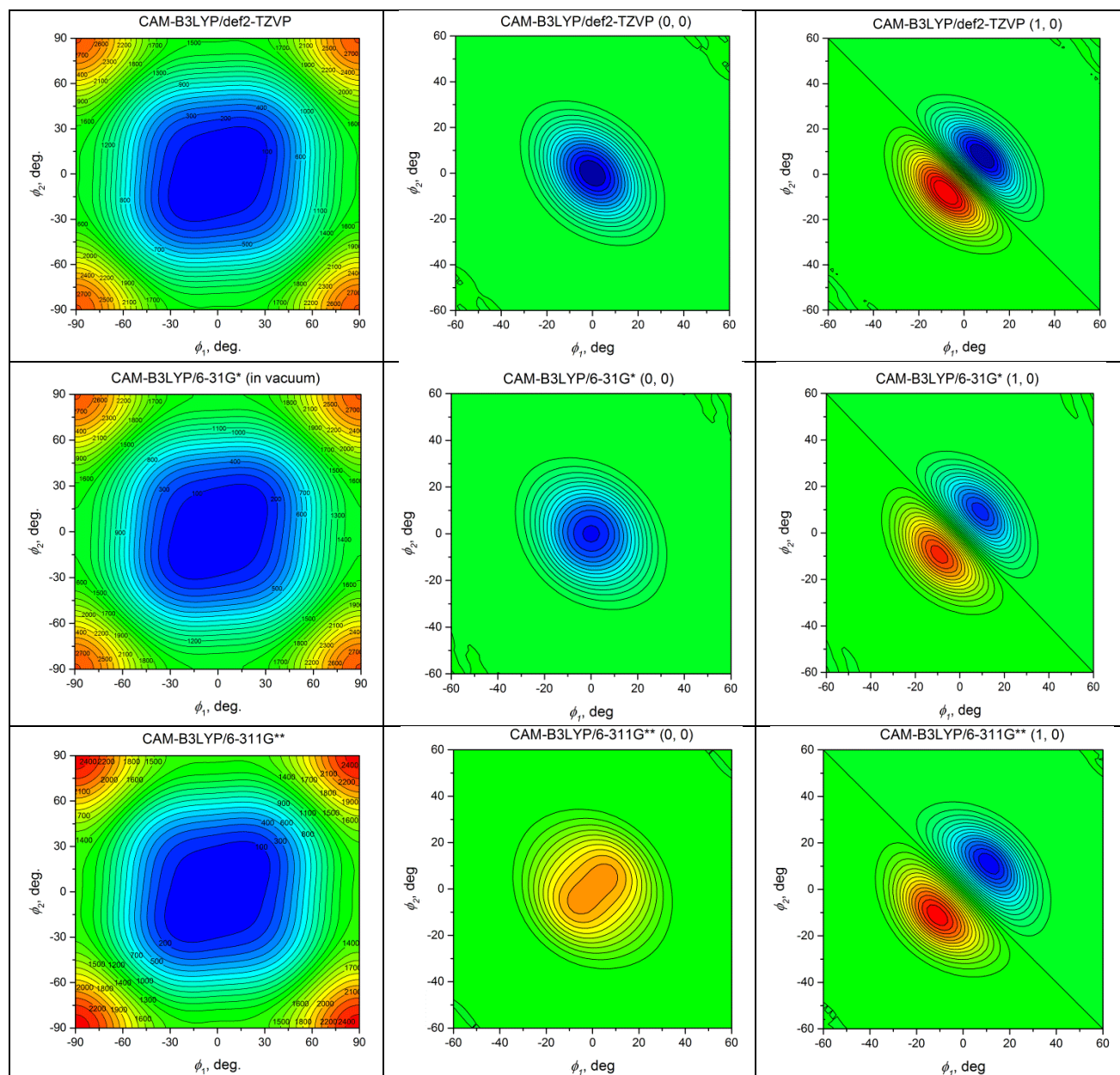


Figure S10c. 2D PES sections along ϕ_1 and ϕ_2 dihedrals and vibrational wave functions obtained for zero and first vibrational levels obtained by CAM-B3LYP functional with different basis sets.

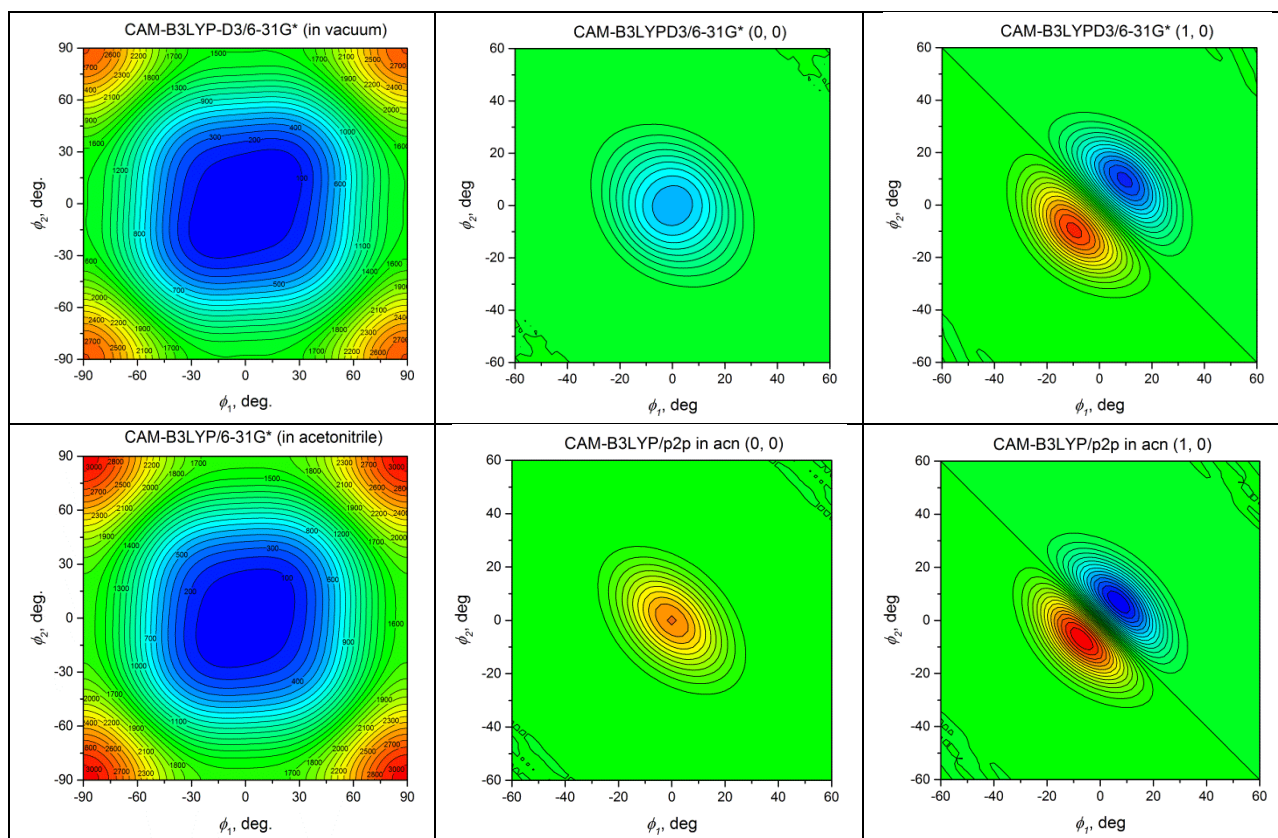


Figure S10d. 2D PES sections along ϕ_1 and ϕ_2 dihedrals and vibrational wave functions obtained for zero and first vibrational levels obtained by CAM-B3LYP/6-31G* basis set with and without dispersion correction and also in acetonitrile.

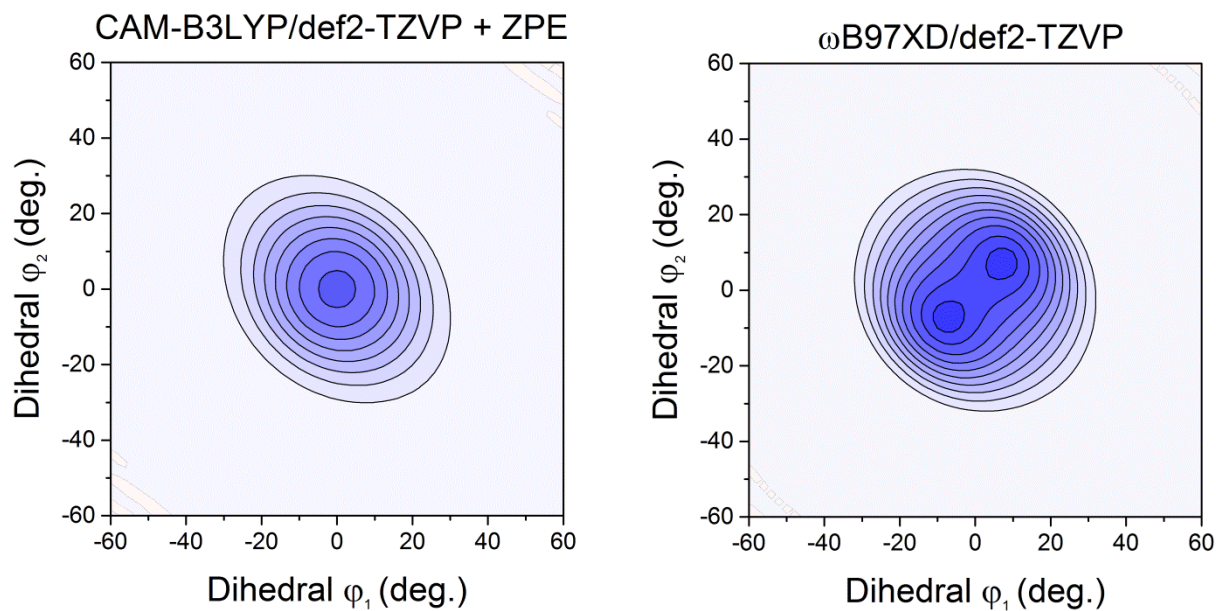


Figure S10e. Ground state vibrational wave-function of trans-stilbene: compare with Figs. 3a,b.

S8. PES in cluster

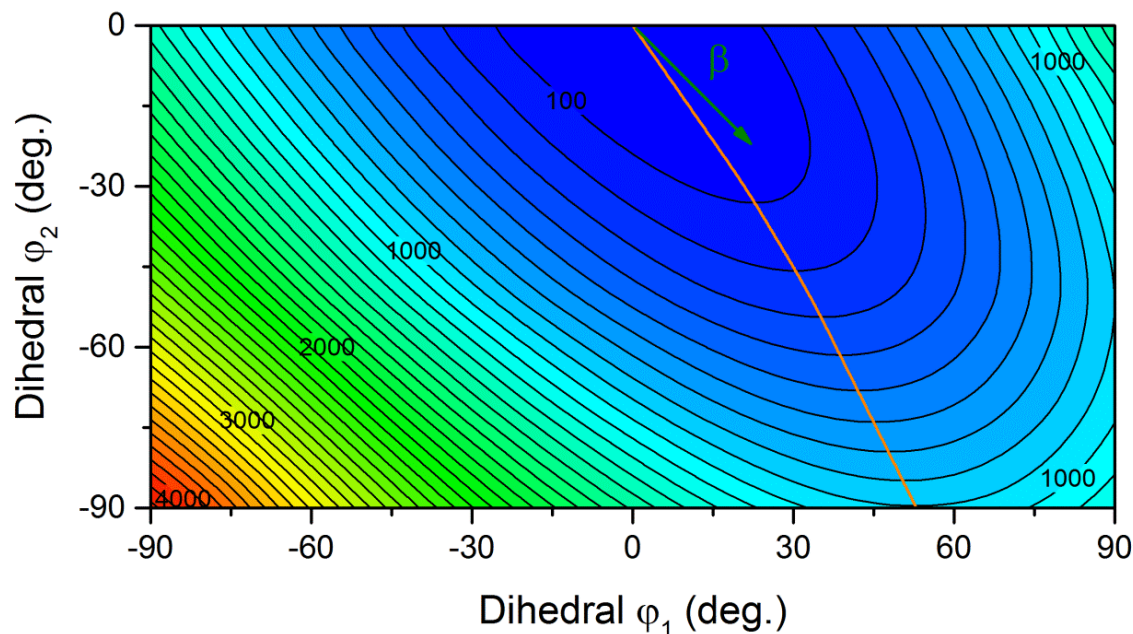


Figure S11. PES of trans-stilbene molecule in rigid crystal (only the studied molecule is relaxed). Numeric labels on the contour lines correspond to energy in meV. Orange curve shows the initial path of a possible pedaling flip of the vinyl group. At large deviations from the planarity, the vinyl hydrogens approach hydrogens of the two neighbor molecules and thus the chosen approximation (only central molecule is fixed) becomes invalid.

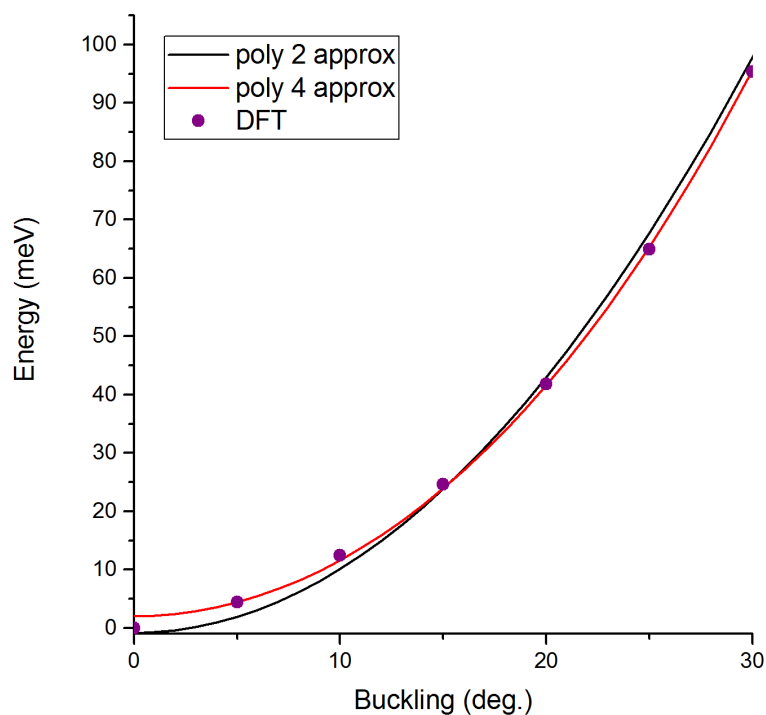


Figure S12. 1D PES section along buckling (β) coordinate for trans-stilbene cluster of 13 molecules: CAM-B3LYP-D3/6-31G* points, harmonic fit, and order-4 polynomial fit.

S9. Vibrational spectra

Table S12. Analysis of Raman-active modes shown in Fig. S8: physical interpretation of modes and calculated frequencies (in cm^{-1}) in vacuum (def2-TZVP basis set) and in crystal (PAW600). Mode numbering includes translations and rotations. The mode at 1200 cm^{-1} is complex involving also C-C single bond stretch. The peaks at 1195 and 1340 cm^{-1} are not isolated well enough for robust cross-identification between gas and crystal phases.

#	Assignment	Experimental frequencies (crystal)	Calculated frequencies			
			vdW-DF2 crystal	CAM-B3LYP gas	PBE-D3 gas	PBE-D3 crystal
40	phenyl rings	997	991	1032	987	992
–	C-H bending	1195	1182	1231	1191	–
–	hydrogens	1340	1352	1383	1317	–
64	BLA on phenyl rings	1595	1562	1680	1592	1587
66	BLA on vinyl group	1642	1617	1739	1639	1635

Table S13. Frequencies of Raman-active phonons of trans-stilbene crystal in low-frequency region ($< 400 \text{ cm}^{-1}$): vdW-DF2 calculations vs experiment. S^A stands for absolute value of Raman scattering factor, S^N - for normalized (for all phonon modes below 400 cm^{-1}).

Mode	Assignment	$\nu_F^{\text{calc}}, \text{cm}^{-1}$	$S^A, \text{\AA}^4/\text{amu}$	S^N	$\nu_F^{\text{exp}}, \text{cm}^{-1}$
6	Rz	38	28.551	2.7	39
7	Rz	42	3.203	0.3	45
12	Rz+Ry	56	27.998	2.6	57
14	Ry+Rz	64	3.136	0.3	63
17	Ry+Rz	73	12.419	1.2	73
20	Ry	87	227.394	21.5	84
28	buckling + Rx	110	142.458	13.5	104
33	Rx + buckling	124	50.973	4.8	123
34	Rx + buckling	127	98.719	9.3	
35	Rx + buckling	129	191.913	18.2	
38	Rx + buckling	133	41.097	3.9	
40	buckling + Rx	146	28.715	2.7	140
45	buckling 2	232	23.137	2.2	229
47	buckling 2	240	40.771	3.9	232
48	buckling 2	248	19.047	1.8	245
55	in-plane bending 3	292	28.490	2.7	293

Table S14. Physical interpretation of low-frequency vibrational modes calculated with explicit elimination of translations and rotations from the force constants matrix of the planar conformer. Modes are numbered according to their CAM-B3LYP/6-31G* energy. This information is used for mode identification for molecule in complex environments and for calculations with different methods. Experimental data are derived from Ref.[32] containing 5 datasets using the following procedure: 1) for some modes we observe that a single data entry is inconsistent with the rest of the data and discard it; 2) the arithmetic average of consistent data is given in the table; 3) if data spread is large we add ' \approx ' symbol; 4) data for buckling are inconsistent and discussed in the text.

#	Energy		Exp. cm ⁻¹	Symmetry		Interpretation
	meV	cm ⁻¹		2/m	mmm	
1	.00	0		Bu	B3u	Tx
2	.00	0		Bu	B2u	Ty
3	.00	0		Au	B1u	Tz
4	-.34	-3		Bg	B3g	Rx (long-axis rotation)
5	-.17	-1		Bg	B2g	Ry (out-of-plane rotation)
6	-.27	-2		Ag	B1g	Rz (in-plane rotation)
7	-1.69	-14	8	Au	Au	torsion (anharmonic 0-1 transition freq. is 7 cm ⁻¹)
8	5.30	43	–	Bg		buckling (anharmonic 0-1 transition freq. is 64 cm ⁻¹)
9	7.43	60	58	Au	B1u	out-of-plane bending (involves phenyl flap)
10	10.24	83	76	Bu	B2u	in-plane bending (involves phenyl wag)
11	25.93	209	202	Ag	Ag	stretching, vinyl angle bending, in-plane bending 2
12	27.34	221	\approx 226	Bg		buckling 2 (involves phenyl flap)
13	36.05	291	291	Ag		in-plane bending 3
14	36.47	294	\approx 285	Au		out-of-plane bending 2
15	52.03	420		Au		torsion 2

Table S15. Vibrational frequencies (in meV) of various systems classified as modes # 1-12 according to Table S13. The default calculation method is indicated in the heading rows. Meaning of labels in the first column is as follows: 'molec' means molecule in vacuum, 'crystal' means Γ -point phonons in crystal with 4 molecules in the unit cell, 'molec 1,2' distinguish two symmetry-nonequivalent molecules in a rigid crystalline environment (force constant matrix of the crystal is cut to the selected molecule), 'm1/c15' means molecule 1 in cluster of 15 molecules cut out of the crystal, 'm1+3/c23' means molecule 1 and 3 in cluster of 23 molecules, 'clf' means chloroform in CPCM model. Phonons labelled by asterisk are mixed with other modes (20% threshold): 1+2+3, 3+9+10, 5+6, 4+8. For example, the eigenfunction of the predominantly buckling mode 16.43* is the superposition of the four molecular vibrations: $\Psi = -0.50\psi_{2,8} - 0.50\psi_{4,8} + 0.46\psi_{2,4} + 0.46\psi_{4,4}$, where the subscripts denote 'molecule.mode', i.e. it intermixes with rotation Rx. Out of the two symmetry nonequivalent molecules, the first molecule has lower buckling and rotation frequencies in consistency with the observation that only this molecule is conformationally disordered in the crystal.

mode #	1	2	3	4	5	6	7	8	9	10	11	12
PBE-D3/PAW600												
6-31G*	0.00	0.00	0.00	0.41	0.09	0.29	1.55	9.37	6.97	9.83	25.06	27.12
def2-QZVP	0.00	0.00	0.00	-0.90	-0.32	0.24	1.44	9.00	6.81	9.62	24.79	26.74
molec	0.01	-0.01	0.00	2.04	-4.50	1.43	3.04	9.32	5.70	9.54	24.71	26.88
molec 1	4.91	6.20	9.23	13.72	9.17	6.43	15.06	15.37	12.73	11.55	25.34	29.41
molec 2	6.22	4.55	8.18	15.88	8.32	5.77	16.01	17.01	11.49	12.77	25.88	30.61
crystal	-0.69*	-0.99	-1.21	13.12*	7.22	4.31	15.11	15.60	8.59*	11.12*	25.25	29.18
	4.56*	4.21*	8.13*	13.59	7.48	5.12	16.24	16.02	12.04*	11.14	25.43	29.57
	5.19*	6.00*	9.84*	14.74*	8.98*	5.60	16.32	16.43*	13.35*	11.59*	25.84	30.08
	6.38	7.42	12.22*	16.11	10.03	7.01*	16.46	18.36	13.74*	13.20	25.91	31.35
vdW-DF2/PAW600												
molec	0.00	0.00	0.00	-0.72	-0.86	-1.07	1.30	9.13	6.53	10.11	25.55	26.84
molec 1	5.29	5.88	9.93	15.17	9.84	5.52	15.04	13.59	12.77	11.26	25.93	29.01
molec 2	5.93	5.50	9.52	15.92	9.69	5.87	15.90	16.75	11.76	12.74	26.32	30.05
crystal	-0.05*	-0.08	-0.19*	15.10*	7.98	4.37	15.09	12.75	9.12*	11.05	25.86	28.69
	4.59*	5.30*	8.64*	15.76	9.02	4.64	16.10	13.62	10.10*	11.36	26.00	29.26
	5.92	6.63	11.55*	15.93	9.07	5.19	16.31	15.40*	11.85*	13.68*	26.28	29.70
	6.23*	7.26	12.61*	16.52*	10.81	6.93	16.57	18.11	13.42*	14.10*	26.32	30.71
CAM-B3LYP-D3/6-31G*												
molec	0.00	0.00	0.00	-0.35	-0.16	-0.27	-1.78	4.82	7.38	10.25	26.05	27.30
m1/c5 in clf*	1.92	5.14	8.10	12.58	7.22	4.09	11.38	10.33	13.52	9.21	26.09	29.55
m1/c5	1.96	5.20	8.03	12.44	7.36	4.06	11.34	10.40	13.51	9.03	26.15	29.43
m1/c11	4.34	7.56	9.82	12.95	9.53	6.78	12.53	12.10	14.52	11.51	26.49	29.85
m1/c13	4.59	7.82	10.83	13.21	10.82	7.76	13.00	12.80	14.91	11.79	26.53	30.20
m1/c15	5.54	8.01	10.64	13.48	10.63	7.73	13.00	12.70	14.84	11.81	26.55	30.07
m1+3/c23	5.51	7.04	10.04	13.50	10.57	7.75	13.11	12.39	14.58	11.88	26.55	30.10
	5.75	8.30	11.04	14.12	10.83	7.85	13.27	13.45	15.76	12.13	26.63	30.18

Table S16. Interpretation of low-frequency Raman active modes. Notation '(XX.yy)' denotes the eigenfunction of yy-th normal mode (see Table S13) of molecule XX in the unit cell (there are four of them). For instance, **I.6** stands for 6th (i.e. Rz) mode of molecule **I**.

#	Energy		Eigenfunction
	meV	cm ⁻¹	
Group of intermixed modes 5+6 (Ry + Rz)			
4	4.37	35	+0.69(III.6)-0.69(I.6)
6	4.64	37	-0.52(I.6)-0.52(III.6)+0.43(II.6)+0.43(IV.6)
7	5.19	42	-0.69(IV.6)+0.69(II.6)
12	6.93	56	0.54(II.6)+0.54(IV.6)+0.37(I.6)+0.37(III.6)+0.25(IV.5)+0.25(II.5)
14	7.98	64	-0.49(III.5)-0.49(I.5)-0.42(IV.5)-0.42(II.5)
16	9.02	73	+0.49(IV.5)-0.49(II.5)-0.48(I.5)+0.48(III.5)
17	9.07	73	-0.47(III.5)-0.47(I.5)+0.46(II.5)+0.46(IV.5)
20	10.81	87	-0.48(II.5)+0.48(IV.5)+0.47(I.5)-0.47(III.5)
Group of intermixed modes 4+8 (Rx + buckling)			
32	15.10	122	-0.42(II.4)-0.42(IV.4)+0.35(III.4)+0.35(I.4)-0.33(IV.8)-0.33(II.8)-0.29(III.8)-0.29(I.8)
33	15.40	124	+0.50(I.4)+0.50(III.4)+0.44(II.8)+0.44(IV.8)
34	15.76	127	-0.62(III.4)+0.62(I.4)+0.26(I.8)-0.26(III.8)
35	15.93	128	+0.65(IV.4)-0.65(II.4)
38	16.52	133	-0.52(II.4)-0.52(IV.4)+0.42(IV.8)+0.42(II.8)
40	18.11	146	-0.65(II.8)+0.65(IV.8)
Intramolecular mode 12 (buckling 2)			
45	28.69	231	-0.65(I.12)+0.65(III.12)-0.26(IV.12)+0.26(II.12)
47	29.70	240	-0.65(II.12)+0.65(IV.12)-0.26(I.12)+0.26(III.12)
48	30.71	248	-0.70(IV.12)-0.70(II.12)

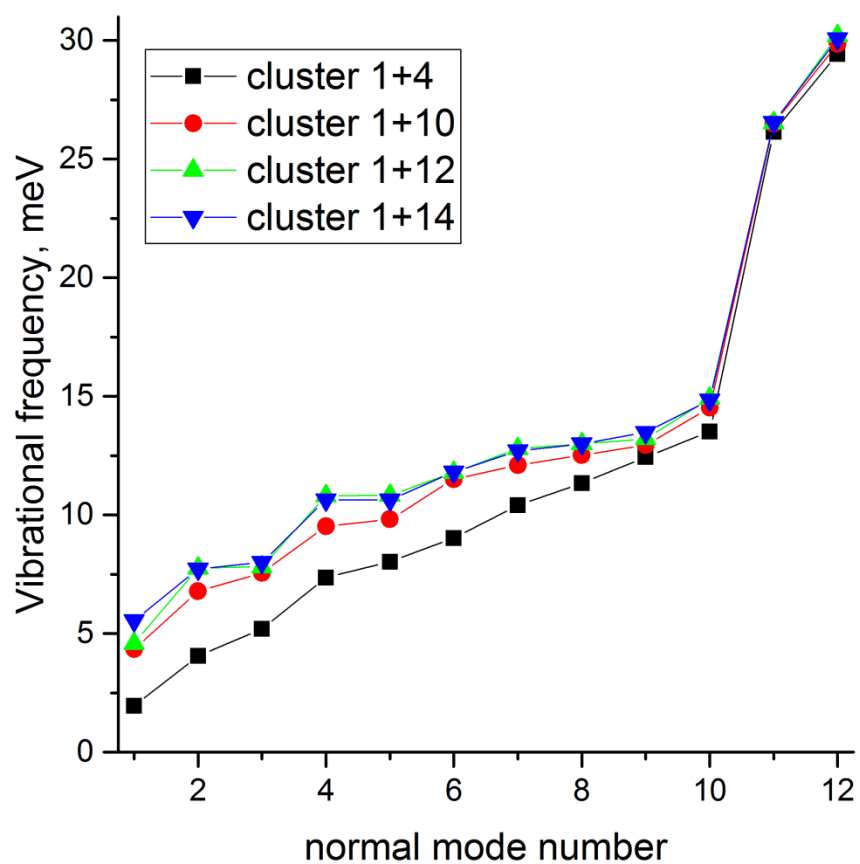


Figure S12x. Convergence of harmonic vibrational frequencies with respect to the cluster size, see Table S15.

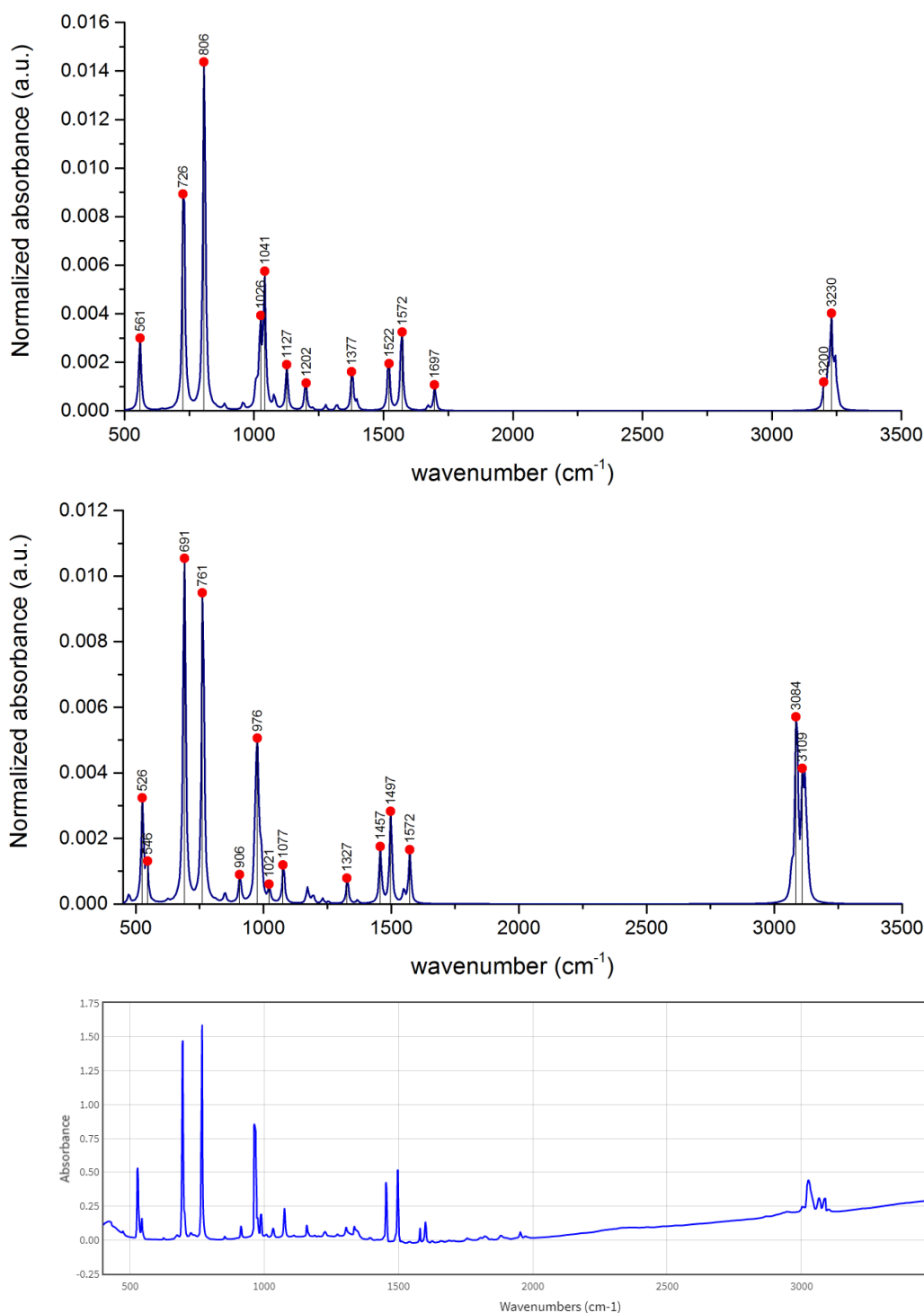


Figure S13. From top to bottom: calculated (CAM-B3LYP-D3/6-31G* and vdW-DF2/PAW600) and experimental (NIST Chemistry WebBook) IR spectra of stilbene crystal. The only notable difference between theory and experiment is the overestimation of intensity of C-H valence vibrations ($>3000\text{ cm}^{-1}$) due to the fact that the absorbance is estimated at 0 K without including temperature effects (i.e. without summation over all levels of the normal mode p , because all transitions with $\Delta v_p = 1$ occur at the same wave number). CAM-B3LYP-D3/6-31G* calculations are performed for a molecule in a rigid cluster of 12 neighbor molecules cut from PBE-D3/PAW600 crystal.

S10. Raman spectra: experimental details and computational analysis

Experimental details. Trans-stilbene powder was purchased from Sigma Aldrich and used as received. Raman spectra were obtained at 83 K using InVia Renishaw spectrometer in conjunction with Leica 2500M confocal microscope. Excitation wavelength was 633 nm. For measuring low-frequency region ($0\text{--}400\text{cm}^{-1}$), built-in double monochromator with subtraction of dispersion (Next, Renishaw) was used; high-frequency measurements were performed with a 633-nm edge filter. To avoid anisotropy effect, spectra were accumulated in several points of the sample (powder pressed in tablet) and then averaged.

Computational methodology. In order to reduce computational cost, Raman intensity calculations were made in vdW-DF2 method rather than in PBE-D3: both show satisfactory agreement with experimental frequencies. The calculated by vdW-DF2 method Raman spectrum is in excellent agreement with experiment. Such a good match is plausibly due to error cancellation: PBE-like methods tend to underestimate frequencies while harmonic approximation usually overestimate them.

Analysis. The peaks with the highest Raman intensity are centered near 997, 1195, 1595, and 1642 cm^{-1} . They correspond to the most Raman-intensive peaks observed in gas phase ([13] and references therein): 1001, 1194, 1600 and 1639 cm^{-1} , also in agreement with calculations, see Table S11. Low frequency region of Raman spectra is more difficult to model due to anharmonism and mode mixing, and the simulated by vdW-DF2 spectrum below 350 cm^{-1} is less accurate than in the higher frequency range, see Fig. S10. Nevertheless, all observed prominent Raman active modes have been identified in the simulated spectrum. In order to interpret Raman-active modes in this region we project their eigenfunctions onto normal modes of individual molecules, which are then matched with normal modes of the free molecule, see Tables S12-S14. One can note that in the dipole approximation odd (A_u and B_u) modes are forbidden by symmetry in Raman spectrum, thus below 200 cm^{-1} symmetrically allowed displacements correspond only to rotations and buckling vibration. Indeed, the analysis of low frequency normal modes (Table S12) reveals that all Raman-active modes below 200 cm^{-1} belong to two groups: the group below 100 cm^{-1} is assigned to molecular rotations R_y and R_z (short axes), whereas other peaks correspond to the intermixed long-axis rotation R_x and buckling. While the phonon frequencies are very close to experimental, the part below 50 cm^{-1} apparently requires more sophisticated techniques evaluating Raman scattering factors (intensities).

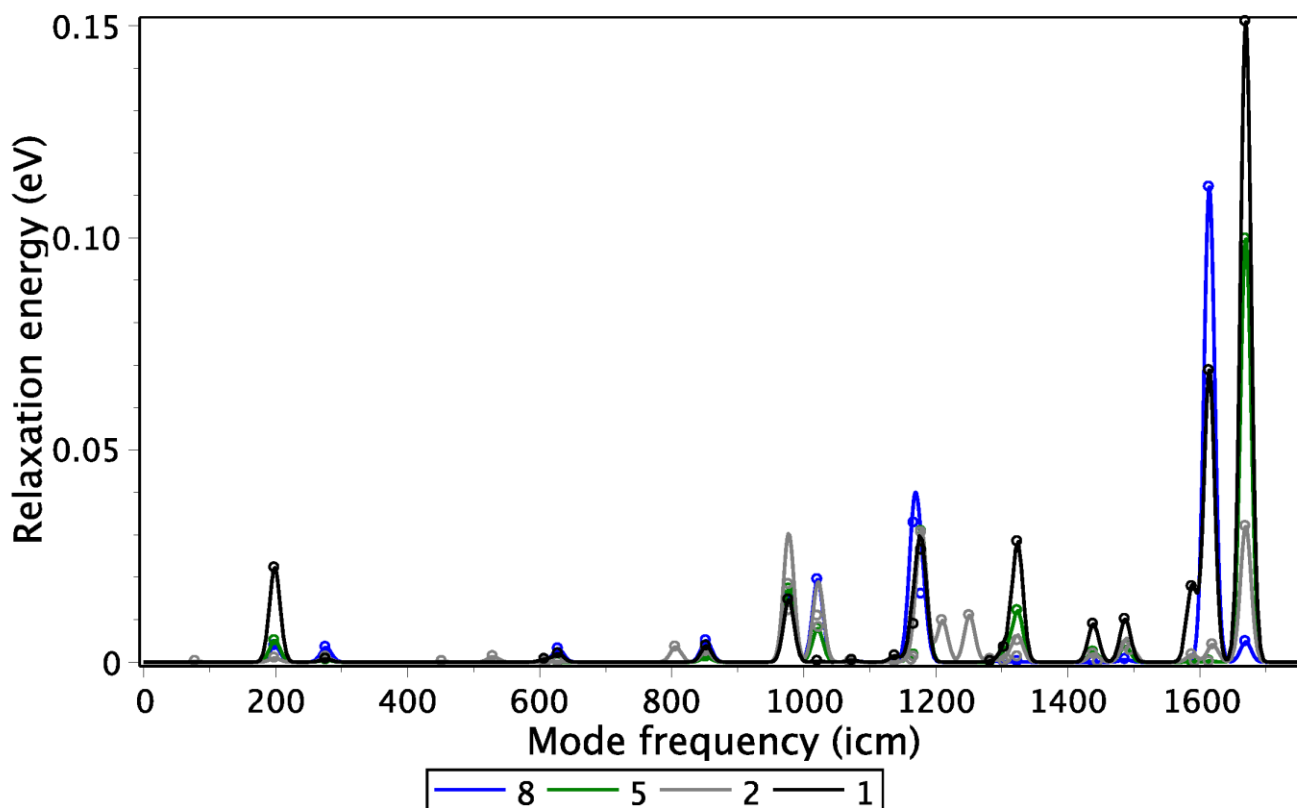


Figure S13x. Linear electron-phonon couplings for all bright excited states of the planar stilbene molecule till 7 eV (see Table S16x) calculated by relaxing the corresponding excitons under $2/m$ symmetry restriction using TDDFT with CAM-B3LYP/6-31G*, see Ref. [5] for the methodology. Plotted are gaussian-broadened relaxation energies $\lambda = S \cdot \hbar \omega$, where S is the Huang-Rhys factor. Then resonance Raman intensities can be estimated by the formula $I_{\omega} \sim \lambda \omega^n d^4 / \Delta \Omega^2$, where 'd' is the transition dipole moment, $\Delta \Omega$ is the deviation from the resonance, and 'n' together with the normalization factor depend on details of the experiment [S19,S20].

Table S16x. Lowest excitations of the planar trans-stilbene calculated by TDDFT with CAM-B3LYP/6-31G*.

#	Energy (eV)	oscillator strength	transition dipole components (e·Å)			sym	Largest CI expansion coefficients	
1	4.38	0.993	-1.25	-1.02	0	BU	48->49	0.70
2	5.11	0.008	0.12	0.07	0	BU	45->51 -0.20, 46->52 -0.20, 47->49 0.47, 48->50 -0.44	
3	5.12	0	0	0	0	AG	45->50 0.21, 46->49 0.47, 47->52 -0.20, 48->51 0.44	
4	5.99	0	0	0	0	AG	45->49 0.49, 46->49 0.27, 48->51 -0.24, 48->52 0.22	
5	6.19	0.344	0.09	-0.79	0	BU	47->49 0.48, 48->50 0.51	
6	6.21	0	0	0	0	AG	45->49 0.41, 46->49 -0.33, 48->51 0.42, 48->52 -0.15	
7	6.32	0	0	0	0	AG	45->49 -0.16, 46->49 -0.23, 48->52 0.58	
8	6.77	0.505	0.74	0.56	0	BU	44->49 -0.21, 45->52 0.17, 46->51 -0.44, 47->50 0.46	
9	7.20	0	0	0	0	BG	39->49 0.15, 41->52 0.16, 42->49 0.16, 43->49 0.63	

S11. Longer oligomers

Table S17. Conformer energies in meV relative to the energy of the lowest conformer ('a'-conformer). The notation 'axN', where N is a number, denotes 'a'-conformer with N pattern defects created (see the main text). The basis set is 6-31G*. Methods predicting fully planar geometry for long oligomers are PBE, B3LYP, HSE06, PW6B95, APF, B2PLYP. Conformers with 'nodata' label exist but have not been calculated, whereas empty cells denote nonexistent conformers.

method	ax1=ax	ax2=dx	ax3=d	planar	b
OPV5					
CAM-B3LYP	0.4	0.9		2.5	
CAM-B3LYP-D3	0.5	nodata		3.3	
M062X	1.6	nodata	4.0	15	
ω B97X	1.0	2.5	3.6	19	
ω B97XD	1.2	nodata	3.8	21	
LC- ω PBE	1.3	nodata	4.3	34	
MP2	2.6	5.1	7.7	92	44
PM7	0.2	1.7	1.4	163	26
OPV3					
CAM-B3LYP	0.5			1.7	
ω B97XD	1.3			12	
MP2	2.5	2.5		51	21
PM7	0.6	0.4		83	13
OPV2					
CAM-B3LYP				1.4	

Table S18. Dependence of lowest vibrational frequencies on oligomer size and method (the basis set is 6-31G). Rows are ordered by the lowest vibration.

Method	IP+EHOMO, eV		Lowest vibrational frequencies for the planar conformer, meV											
OPV5														
PW6B95	0.83	0.78	1.07	1.13	1.53	1.82	2.59	2.64	3.80	5.41	7.85	7.92	9.14	
PBE	1.23	0.61	1.23	1.45	1.58	2.42	2.43	3.41	4.08	4.18	7.77	7.79	8.55	
PBE-D3	1.23	0.60	1.22	1.41	1.59	2.36	2.39	3.34	4.04	4.19	7.71	7.82	8.46	
HSE06	1.11	0.47	0.79	0.96	1.54	1.65	1.95	2.67	3.95	4.32	7.94	8.03	8.18	
B3LYP	0.94	0.33	0.96	1.01	1.55	1.76	2.15	2.78	4.01	4.24	7.97	7.99	8.35	
APF	0.89	-0.27	-0.22	0.67	1.25	1.60	1.61	2.52	3.84	4.28	7.83	7.96	7.98	
PBE0	0.86	-0.71	-0.68	0.38	1.08	1.37	1.62	2.43	3.77	4.29	7.76	7.85	8.02	
APFD	0.89	-1.00	-0.99	-0.16	0.88	1.08	1.65	2.37	3.64	4.37	7.50	7.52	8.15	
CAM-B3LYP	0.25	-1.51	-1.48	-0.96	-0.55	1.02	1.59	2.23	3.26	4.31	6.77	6.79	8.10	
CAM-B3LYP-D3	0.25	-1.67	-1.60	-1.09	-0.59	1.00	1.59	2.16	3.12	4.32	6.48	6.50	8.11	
M062X	0.43	-2.53	-2.22	-1.35	0.35	1.36	1.64	1.99	2.13	4.70	4.70	4.70	6.73	
ωB97X	-0.37	-2.93	-2.59	-2.12	-1.70	-1.07	-0.26	0.52	1.83	2.40	2.63	4.52	5.08	
ωB97XD	-0.19	-3.22	-2.81	-2.30	-1.96	-0.91	0.41	0.58	1.72	2.65	3.08	4.40	5.33	
LC-ωPBE	-0.48	-4.30	-4.18	-3.19	-2.86	-2.58	-2.23	-1.73	-0.87	1.12	1.68	3.84	4.37	
OPV3														
PBE	1.68	1.27	2.50	2.54	4.52	7.45	9.24	10.55	12.11	18.01	23.24	23.36	29.89	
B3LYP	1.27	0.71	1.68	2.53	4.57	7.70	8.69	10.82	10.92	18.44	23.28	23.92	30.60	
CAM-B3LYP	0.35	-1.72	-1.09	2.26	4.66	6.63	6.86	8.45	11.00	18.67	22.37	24.23	30.63	
ωB97XD	-0.15	-3.02	-2.31	-0.70	-0.50	4.42	4.75	8.02	10.96	18.57	21.35	24.11	29.96	
OPV2 (stilbene)														
PBE	2.13	1.63	7.01	9.57*	9.80	24.90	27.15	34.18	34.83	49.05	49.22	56.86	56.98	
B3LYP	1.60	0.84	7.29	8.50*	10.08	25.58	27.59	35.66	35.70	51.18	51.32	58.70	59.23	
CAM-B3LYP	0.49	-1.69	5.30*	7.43	10.24	25.93	27.34	36.05	36.47	52.03	52.13	59.03	60.06	
ωB97XD	-0.05	-2.95	-2.16*	7.36	10.44	25.62	26.49	36.11	36.16	51.48	51.56	59.19	59.39	

* Buckling mode (note that mode ordering can be different for different methods).

Table S19. Calculated vs. experimental geometry of stilbene (OPV2), 1,4-bis(4-methylstyryl)benzene (OPV3-Me), OPV5 and PPV. Computed structures for OPV2 are dynamically stable, i.e. there is no imaginary vibrational frequencies at Γ -point and no negative eigenvalues of the elastic tensor. Computed PPV and OPV3-Me structures are unstable with respect to unit cell symmetry lowering. For OPV5 such analysis is computationally challenging.

Method	Unit cell volume per atom, Å ³	Lattice constants, Å			β, deg.	
		a	b	c		
OPV2, space group is P2 ₁ /a						
PBE-MBD	9.38	12.232	5.621	15.309	112.13	
PBE-D3	9.41	12.231	5.600	15.400	111.97	
experiment at 90 K [23]	9.56	12.276	5.657	15.442	112.04	
VDW-DF2	9.85	12.367	5.707	15.638	111.86	
OPV3-Me, space group is Pbca						
PBE-D3	9.04	7.317	5.844	38.887	90	
experiment at 123 K [24]	9.17	7.362	5.883	38.950	90	
vdW-DF2	9.50	7.489	5.960	39.147	90	
OPV5, space group is P2 ₁ /a						
PBE-D3	9.19	15.786	7.434	32.889	103.74	
experiment at 220 K [20]	9.51	16.072	7.538	32.914	103.35	
vdW-DF2	9.70	15.986	7.690	33.072	103.23	
PPV, space group is P2 ₁ /c						
PBE-D3	9.19	6.675	7.613	6.037	122.94	
experiment [21]	9.42	6.58	7.90	6.05	123.	
vdW-DF2	9.61	6.712	7.806	6.112	122.8	

S12. Electronic couplings and band structure

Table S20. Comparison table of hopping amplitudes (see caption of Table S21) for electrons and holes in stilbene (OPV2), 1,4-bis(4-methylstyryl)benzene (OPV3-Me), and OPV5 vs. electrons in TCNQ and F₂-TCNQ. Geometry is fully relaxed by PBE-D3, electronic couplings are calculated by CAM-B3LYP/6-31G*. The 'bandwidth' is defined here as the mean square deviation of band energies.

crystal		hopping amplitudes (eV·Å)			bandwidth (eV)	band span (eV)	μ (cm ² /Vs)	ref
F ₂ -TCNQ	electrons	0.94	0.39	0.38	0.18	1.02	6-7	[52]
TCNQ	electrons	0.45	0.32	0.31	0.14	0.65	1.6, \approx 0.1	[51,52]
OPV2	holes	0.40	0.30	0.19	0.11	0.51	–	
OPV2	electrons	0.38	0.33	0.16	0.12	0.53	–	
OPV3-Me	holes	0.23	0.22	0.04	0.09	0.37	0.01	[24]
OPV3-Me	electrons	0.44	0.38	0.04	0.17	0.63	0.1	[24]
OPV5	holes	0.20	0.15	0.06	0.08	0.32	–	
OPV5	electrons	0.27	0.26	0.04	0.11	0.42	–	

Table S21. Transfer integrals (intermolecular couplings) and efficiencies for electrons and holes in stilbene crystal fully relaxed by PBE-D3. Here 'mol1' and 'mol2' are the two molecules participating in the transfer. There are 4 molecules in the unit cells numbered from 1 to 4. For 'mol2' the notation 'm n1 n2 n3' means molecule 'm' translated by n1 unit cells along the first translation vector, by n2 along the second translation vector, and by n3 along the third vector. Only symmetry nonequivalent dimers are listed, their multiplicity per unit cell is given in 'mul' column. The distance 'a' is the center-to-center (hopping) distance. The transfer efficiency is the product $t^2 a^2$ given in eV²Å² and is proportional to the contribution of the given transfer to the charge carrier mobility along the direction of the transfer. The three eigenvalues of the charge carrier mobility tensor are proportional to the *hopping amplitudes* which are equal (in eV·Å) to 0.38, 0.33, 0.16 for electrons and 0.40, 0.30, 0.19 for holes.

mol1	mol2	mul	t(meV)	a(Å)	eff.
electrons					
2	2 0 1 0	4	68	5.6	0.145
2	4 0 1 0	8	-47	6.7	0.099
1	1 0 1 0	4	54	5.6	0.092
1	2 0 0 -1	8	-21	8.2	0.029
1	3 0 0 0	8	-24	6.7	0.026
1	4 0 0 0	8	6	7.8	0.002
1	2 0 0 0	8	-4	8.2	0.001
holes					
2	4 0 1 0	8	49	6.7	0.107
1	4 0 0 0	8	-37	7.8	0.086
1	3 0 0 0	8	36	6.7	0.059
1	2 0 0 -1	8	-20	8.2	0.027
1	1 0 1 0	4	18	5.6	0.010
1	2 0 0 0	8	-7	8.2	0.004
2	2 0 1 0	4	5	5.6	0.001

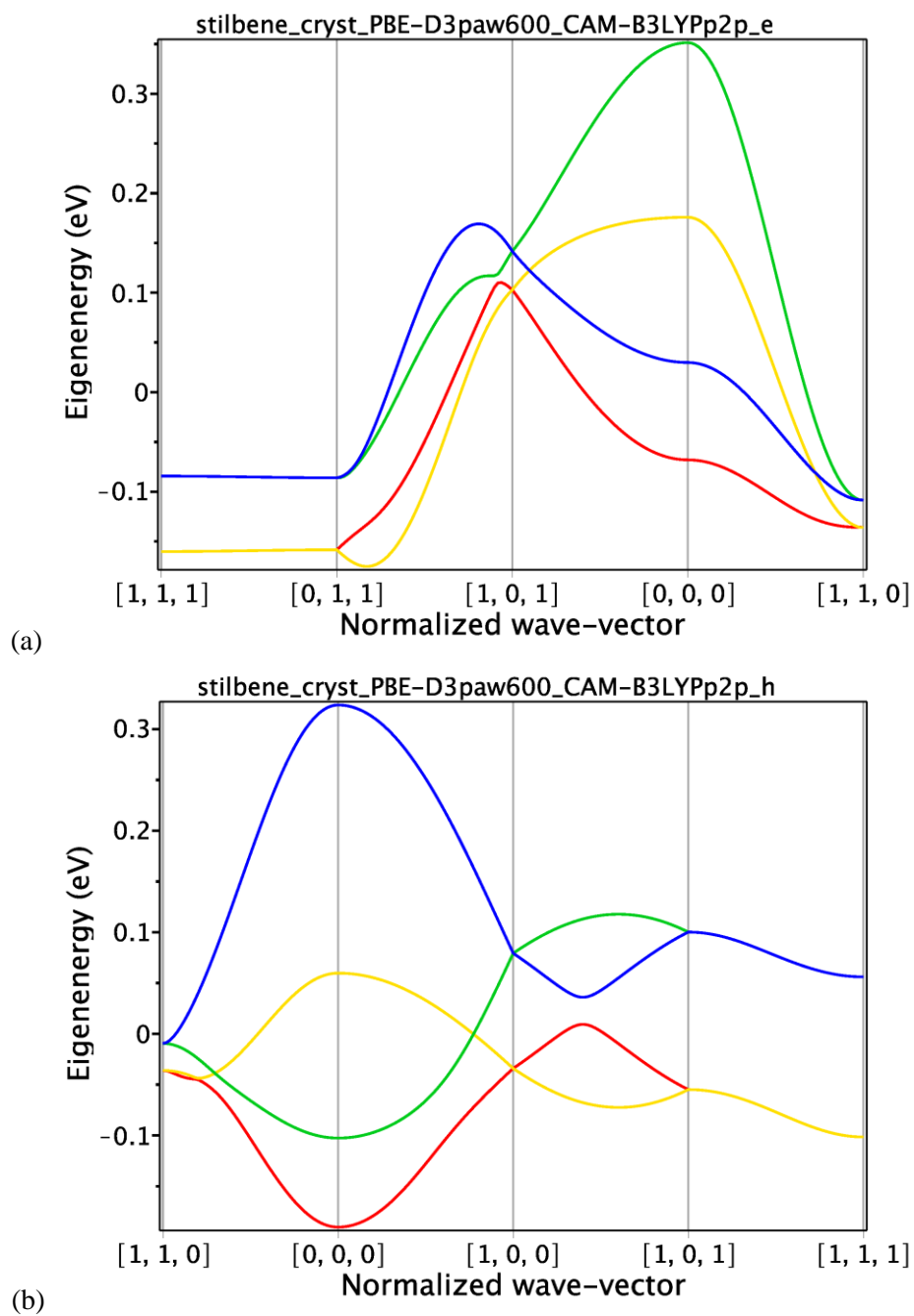


Figure S14. Band structure for electrons (a) and holes (b) in stilbene.

Table S22. Transfer integrals (intermolecular couplings) and efficiencies for electrons and holes in OPV5 crystal fully relaxed by PBE-D3. Here 'mol1' and 'mol2' are the two molecules participating in the transfer. There are six molecules in the unit cells numbered from 1 to 6. The three eigenvalues of the charge carrier mobility tensor are proportional to the hopping amplitudes which are equal (in eV·Å) to 0.27, 0.26, 0.04 for electrons and 0.20, 0.15, 0.06 for holes.

mol1	mol2		mul	t(meV)	a(Å)	eff.
electrons						
2	5	0 0 0	8	70	6.5	0.210
2	3	0 0 0	4	64	6	0.145
1	2	0 1 0	8	-49	4.7	0.053
1	2	0 0 0	8	17	4.8	0.007
1	2	0 1-1	8	1	31.8	0.002
2	3	0 0 1	4	-1	30.4	0.001
holes						
2	5	0 0 0	8	-62	6.5	0.163
2	3	0 0 0	4	27	6	0.027
1	2	0 0 0	8	-26	4.8	0.015
1	5	0 0 0	8	-13	6.1	0.006
2	3	0 0 1	4	2	30.4	0.003
1	2	0 1 0	8	-9	4.7	0.002
1	2	0 0-1	8	-1	31.8	0.002
1	2	0 1-1	8	-1	31.8	0.002
2	5	0 0 1	8	-1	28.5	0.001

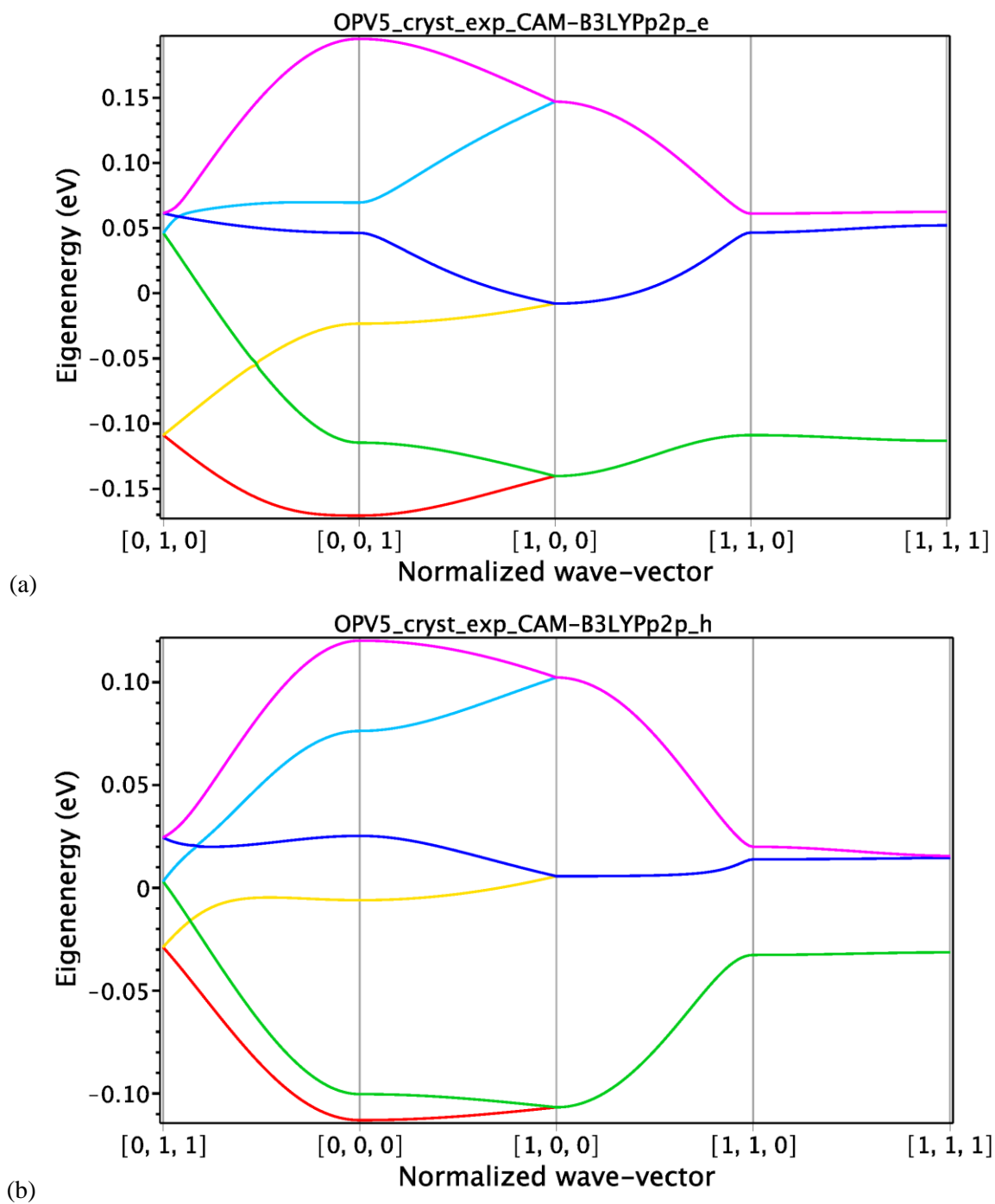


Figure S15. Band structure for electrons (a) and holes (b) in OPV5 crystal (experimental geometry).

References

- S1. NIST Computational Chemistry Comparison and Benchmark Database, DOI:10.18434/T47C7Z
- S2. The WSPC Reference on Organic Electronics, ed J L Bredas, S R Marder (WSPC, 2016), p.35
- S3. Arenas, J. F.; Tocón, I. L.; Otero, J. C.; Marcos, J., A Priori Scaled Quantum Mechanical Vibrational Spectra of trans- and cis-Stilbene. *J. Phys. Chem.* **1995**, 99, 11392-11398.
- S4. Negri, F.; Orlandi, G., Infrared and Raman Spectra of Binuclear Aromatic Molecules: A Density Functional Theory Study. *J. Raman. Spectrosc.* **1998**, 29, 501-509.
- S5. Wernecke, W.; Pfeiffer, M.; Johr, T.; Lau, A.; Jiipner, H.-J., Electronic and Raman-type nonlinearities of thin films of oligomeric paraphenylene vinylenes. *Chem. Phys.* **1995**, 199, 65-72.
- S6. Zerbi, G., Vibrational Spectroscopy of Conducting Polymers: Theory and Perspective, in "*Handbook of Vibrational Spectroscopy*", John Wiley & Sons, Ltd., **2007**.
- S7. Melandri, S.; Maccaferri, G.; Favero, P. G.; Caminati, W.; Orlandi, G.; Zerbetto, F. Stilbenoid molecules: An Experimental and Theoretical Study of trans-1-(2-pyridyl)-2-(4-pyridyl)-ethylene and the Parent Molecule. *J. Chem. Phys.* **1997**, 107, 1073-1078.
- S8. Meic, Z.; Gusten, H., Vibrational studies of trans-stilbenes---I. Infrared and Raman spectra of trans-stilbene and deuterated trans-stilbenes, *Spectr. Acta* **1978**, 34A, 101-111.
- S9. Carreira, L.A.; Towns, T.G., Determination of the torsional potential function for styrene, *J. Chem. Phys.* **1975**, 63, 5283-5286.
- S10. Jacquemin, D.; Adamo, C., Bond length alternation of conjugated oligomers: wave function and DFT benchmarks, *J. Comp. Theor. Chem.* **2011**, 7, 369.
- S11. Nayyar, I.H.; Batista, E.R.; Tretiak, S.; Saxena, A.; Smith, D.L.; Martin, R.L., Role of Geometric Distortion and Polarization in Localizing Electronic Excitations in Conjugated Polymers. *J. Chem. Theory Comput.* **2013**, 9, 1144.
- S12. Fonari, A.; Stauer, S., vasp raman.py; <https://github.com/ramansc/VASP/>, **2013**.
- S13. Harthcock, M.A.; Laane, J., Calculation of kinetic energy terms for the vibrational Hamiltonian: Application to large-amplitude vibrations using one-, two-, and three-dimensional models. *J. Mol. Spectrosc.* **1982**, 91, 300.
- S14. Harthcock, M.A.; Laane, J., Calculation of two-dimensional vibrational potential energy surfaces utilizing prediagonalized basis sets and Van Vleck perturbation methods. *J. Phys. Chem.* **1985**, 89, 4231-4240.
- S15. Adler, T.B.; Werner, H.J., An explicitly correlated local coupled cluster method for calculations of large molecules close to the basis set limit. *J. Chem. Phys.* **2011**, 135, 144117.
- S16. Celebre, G.; De Luca, G.; Di Pietro, M.E., Conformational Distribution of trans-Stilbene in Solution Investigated by Liquid Crystal NMR Spectroscopy and Compared with in Vacuo Theoretical Predictions, *J. Phys. Chem. B* **2012**, 116, 2876-2885.
- S17. Hollas, J.M.; Ridley, T., The A1A'-A1A' single vibronic level fluorescence spectrum of styrene vapor, *J. Mol. Spectrosc.* **1981**, 89, 232-253.
- S18. Abraham, M.H.; Green, C.E.; Acree Jr., W.E.; Hernandez, C.E.; Roy, L.E., Descriptors for solutes from the solubility of solids: trans-stilbene as an example. *J. Chem. Soc., Perkin Trans.* **1998**, 2, 2677-2681.
- S19. McHale, J., Molecular Spectroscopy (CRC, **2017**).
- S20. Peticolas, W.L.; Blazej, D.C., Estimation of the distortion of the geometry of nucleic-acid bases in the excited electronic state from the ultraviolet resonance Raman intensity of certain normal modes, *Chem. Phys. Lett.* **1979**, 3, 604.